Università degli Studi di Cassino e del Lazio Meridionale
Corso di Dottorato in Metodi, Modelli e Tecnologie per l'Ingegneria
Dipartimento di Ingegneria Civile e Meccanica

RICHTMYER-MESHKOV INSTABILITY FOR THE ANALYSIS OF MATERIALS AT HIGH STRAIN RATES

Mirko Sgambetterra

mirko.sgambetterra@unicas.it

In Partial Fulfillment of the Requirements for the Degree of
PHILOSOPHIAE DOCTOR in
Mechanical and Management Engineering

09/12/2025

TUTOR
Prof. Testa
Prof. Bonora

COORDINATOR
Prof. Marignetti

UNIVERSITÀ DEGLI STUDI DI CASSINO E DEL LAZIO MERIDIONALE

CORSO DI DOTTORATO IN METODI, MODELLI E TECNOLOGIE PER L'INGEGNERIA

Date: **09/12/2025**

Author: **Mirko Sgambetterra**

Title: **RICHTMYER-MESHKOV INSTABILITY FOR THE ANALYSIS OF MATERIALS AT HIGH STRAIN RATES**

Department: **DIPARTIMENTO DI INGEGNERIA CIVILE E MECCANICA**

Degree: **PHILOSOPHIAE DOCTOR**

To Ivan

a brother, an engineer, a light that still inspires me

Acknowledgements

I would like to express my sincere gratitude to my supervisors, Prof. Gabriel Testa and Prof. Nicola Bonora, for their continuous guidance and support throughout this work. I am also thankful to the entire research group at the University of Cassino for their collaboration and assistance during the development of this thesis.

I would also like to express my appreciation to Italian Air Force for its opportunity, and in particular to Guido, whose mentorship and thoughtful guidance, both throughout this project and in my broader professional growth, have been truly invaluable.

Finally, I am deeply grateful to my family, my parents, Igor and his family, and the family I have found alongside Chiara, for their constant encouragement, support, and understanding throughout this journey.

Contents

List of Figures

List of Tables

Abstract

The mechanical resistance of a metal, as the strain rate increases, undergoes a significant increase in the range between 10^3 and $10^5\,s^{-1}$ caused by the transition from a thermally activated mechanism to a viscous regime of the dislocations' motion. In this regime, it is still possible, albeit with some difficulty, to obtain reliable high-strain-rate flow stress data from a small-scale Hopkinson bar test. Beyond this threshold, it is necessary to resort to impact compression experiments, which, however, generate very high pressures that do not allow for a straightforward estimation of the strain rate effect.

The relatively low pressure obtained through Richtmyer-Meshkov instability (RMI) experiments has led to this technique receiving considerable attention in recent years. In RMI experiments, it has been demonstrated both theoretically and experimentally that the strain rate for a given impact is inversely proportional to the wavelength of the sinusoidal perturbations, provided the amplitude-to-wavelength ratio remains constant. Typically, in an experiment conducted with a gas gun, it is possible to obtain a strain rate greater than $10^7\,s^{-1}$ with a perturbation wavelength of approximately $100\,\mu m$.

The material models used in the simulations can be validated by comparing both the deformation and the growth velocity of the spikes, which is a velocity measured experimentally using Photon Doppler Velocimetry (PDV).

Spikes with a relatively small area can be a problem for both velocity measurement with PDV and post-mortem analysis. To overcome this limitation and modulate the strain rate, the application of RMI experiments was explored to investigate the mechanical response of annealed copper with perturbations larger than those reported in the literature.

Numerical simulations were conducted using an implicit finite element code to demonstrate the feasibility of this study and to identify the limitations of the technique to extract accurate velocity data and fragments with manageable dimensions. In the simulation, a material model that includes an increase in resistance with varying strain rate was used. The numerical simulations indicated that the material points along the longitudinal axis represent various stages of a deformation history, taking into account the temperature effect.

Subsequently, different geometries were selected from numerical simulations, and the test was conducted. The experimental results were compared with those obtained from the simulations.

Introduction

Understanding how materials behave under extreme conditions, characterized by phenomena such as shock compression, high strain rates, intense pressures, and elevated temperatures, is of great importance in different scientific and engineering disciplines, such as mining, aerospace, defense, energy storage and production, astrophysics, and geology.

In mining, understanding the dynamic mechanical behavior of minerals and ores is crucial for safety and stability [1] [2]. In the civilian aerospace industry, this knowledge is essential in order to design crash-resistant structures, in the event of a bird strike or hail impact on the aircraft, ensuring structural integrity and passenger safety [3] [4] When it comes to military aviation, understanding how materials respond to blast loads is absolutely crucial for aircraft survival [5]. In ballistics, it is indispensable to assess the impact resistance of armor materials. In fact, the mechanisms of deformation of the targets when struck by projectiles can lead to the development of more effective protective gear and systems [6]. In energy production through inertial confinement fusion, precise control over the implosion of shock-accelerated fuel layers is absolutely critical [7], meanwhile, it is important in the interpretation of astrophysical phenomena such as supernova explosions [8] or in geology, in the analysis of hydrogeological changes induced by earthquakes [9].

Characterizing the mechanical and thermodynamic properties of materials at elevated pressure, strain level, strain rate, and temperature presents considerable experimental and computational challenges. Although material behavior is well understood under ambient conditions, predicting its response at these extremes remains a complex undertaking. The combined influence of strain, strain rate, temperature, and pressure on a material's strength (and its underlying deformation mechanisms) necessitates the improvement of predictive models, techniques capable of providing the data to populate them, and independent validation methodologies.

Constitutive laws (or models) are mathematical relationships designed to quantitatively describe the mechanical behavior of materials under the conditions mentioned above. The accuracy and predictive capability of simulations are directly contingent upon the precision of the underlying constitutive models in representing the material's deformation response.

In order to test material at high strain rate a split-Hopkinson bar (Kolsky bar) test [10] is commonly used for determining the dynamic mechanical properties of many materials, including metals. The rate achievable with this technique range from 10^2 to $10^4\, s^{-1}$, but can exceed $10^5\ \ s^{-1}$ with miniaturized samples [11].
With the aim of achieving higher strain rates and larger strains, plate impact tests have been developed. These experiments can generate extremely high pressures, often exceeding several Gigapascals [12], due to the shock loading nature of the test. While such conditions are useful for investigating material behavior under extreme environments, alternative testing methods are more suitable to study the material response in regimes where deformation mechanisms are activated by strain rather than pressure, avoiding phase transformations or damage phenomena driven primarily by shock-induced pressure.

In recent years Richtmyer–Meshkov Instability (RMI) phenomenon applied to solids has been increasingly used as a diagnostic tool to probe the dynamic strength and constitutive behavior of materials subjected to extreme loading conditions [13]. To achieve lower impact pressures while still maintaining high levels of strain and strain rate, modifications have been introduced to the experimental configuration of the RMI. In this thesis work, such modifications were first investigated numerically and subsequently validated through experimental data.

To guide the reader through the development of this work, the thesis is structured as follows: Chapter 1 provides a background on the main constitutive models used to describe the behavior of metals under shock loading, including mechanical tests and their limitation, introducing the motivation of the RMI test and the modification proposed by this work. Chapter 2 presents the experimental setup of this study. It describes the configuration of the RMI experiments, diagnostic techniques, and the parameters

of interest. In addition, it presents the results of the numerical simulations and their comparison with experimental data. The ability of various constitutive models to reproduce observed instability growth and material response under shock loading is critically assessed.

Chapter 3 offers a discussion of the findings, highlighting the implications for material modelling at high strain rates, the sensitivity of RMI growth to strength parameters, and the potential of RMI-based methods for validating constitutive behaviour in solid materials.

Finally, will be summarizes the main conclusions of the work and outlines possible directions for future research, including improvements to experimental design, model refinement, and broader applications of RMI-based strength characterization.

Chapter 1

Background

1.1 Theoretical background

While mechanical tests provide invaluable data, interpreting these results requires a theoretical background that captures the underlying physics of plastic deformation. This is commonly expressed through constitutive models, which provide mathematical relationships between stress, strain, strain rate, and temperature, describing phenomena such as strain and strain rate hardening, as well as thermal softening.

Before introducing constitutive laws, it is necessary to discuss the fundamental mechanisms that govern plastic deformation in metals. In particular, the role of dislocations as carriers of plastic strain provides the foundation for understanding the material behavior for different deformation regimes.

1.1.1 Dislocations and plastic strain

In 1934, Orowan, Polanyi, and Taylor [14, 15, 16] independently and concurrently introduced the concept of line defects within a crystal structure that provide a consistent explanation for the lower shear stresses observed experimentally with respect to the theoretically calculated ones. Dislocation is indeed the mechanism for accommodating permanent (plastic) strain[1].

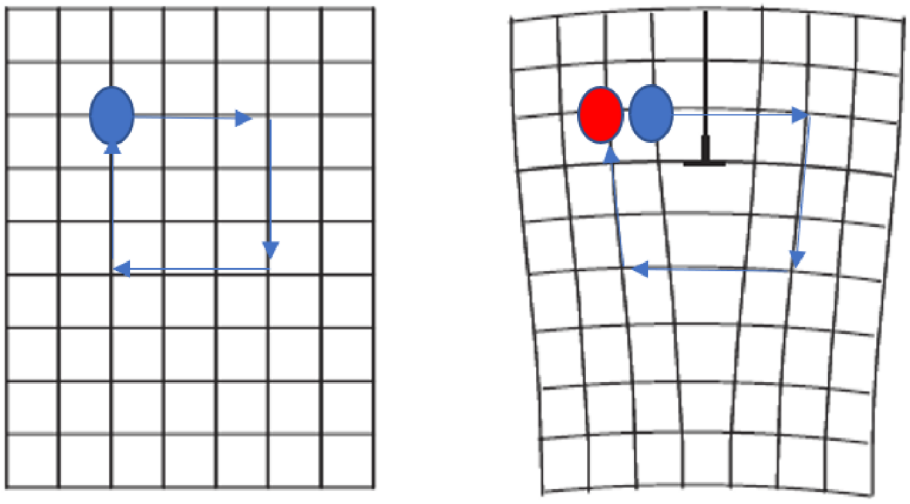

Figure 1.1: Graphical representation of an edge dislocation. The vector connecting the blue circle (initial position) and the red circle (final position) is the Burgers vector.

In Figure 1.1, a comparison is shown between a perfect crystal lattice, on the left, and one containing an edge dislocation, on the right. An edge dislocation consists of a half-plane of atoms inserted into the crystal lattice, which distorts the surrounding atomic arrangement over a region referred to as the *dislocation width*, w. In the perfect lattice, a closed circuit can be constructed: for example, by taking three steps to the right and three steps downward, each step corresponding to one lattice spacing, and then completing the loop, the path ends exactly at the starting point, see the blue arrows and circle in

[1] The total strain experienced by a material under load can be decomposed into two contributions: an elastic component ε_{el}, which is fully recoverable upon unloading, and a plastic component (ε_p), which represents the permanent deformation.

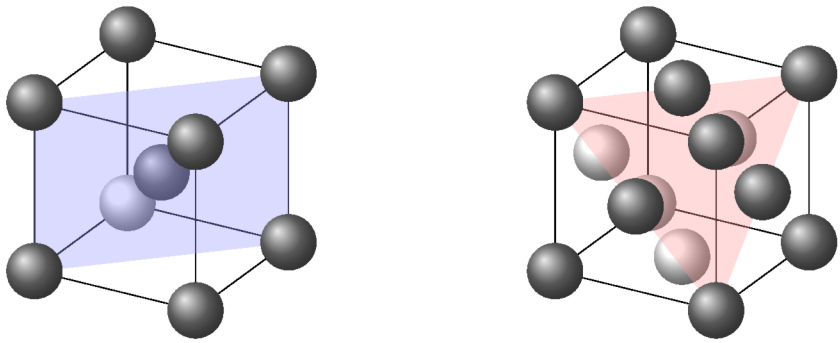

Figure 1.2: Crystal structures of a Body-Centered Cubic (BCC) and a Face-Centered Cubic (FCC) lattice, each with one slip plane indicated: the (110) plane for BCC and the (111) plane for FCC.

the left panel. In contrast, when the same circuit is drawn around a lattice with a dislocation, the path does not close. Instead, it terminates at a different position, shifted by the extra half-plane of atoms. The vector needed to connect the final point to the starting point is the Burgers vector (**b**). The number of dislocations in a metal can roughly vary from 10^3 of an annealed one up to 10^{12} in a heavily deformed one. The number of dislocations per unit of volume is defined as dislocation density ρ_d.

Orowan equation, in a time-integrated form, describes the amount of strain that dislocations achieve by their motion:

$$\varepsilon = \rho_d \, b \, l \tag{1.1}$$

where ε is the true strain[2], ρ_d is the dislocation density, b is the Burgers vector, and l is the distance moved by dislocations.

The Orowan equation directly implies that any mechanism that hinders the movement of dislocations increases strength, such as intrinsic resistance to motion of the crystalline lattice [18] (*Peierls* stress), grain boundaries [19, 20], solution and precipitation hardening [21], and stored dislocations.

To introduce the intrinsic resistance to dislocation motion in a crystal lattice, two typical cubic structures are shown in Figure 1.2.

Dislocations tend to glide along specific planes, known as slip planes, which correspond to the planes of highest atomic density. These planes are energetically favorable because atoms are closely packed, allowing the dislocation to move with less resistance. Indeed, suppose a stack of spheres is taken as a representation of atomic planes, on a dense plane (close-packed). In that case, the spheres are closely aligned, allowing a row to be displaced with minimal disturbance to the surrounding atoms. In contrast, on a less dense plane, the spheres are more widely spaced and irregular, making it more challenging to move a row and requiring greater applied stress.

The planes with maximum atomic density are highlighted in Figure 1.2, for the motivation mentioned above that dislocations preferentially glide along these planes (Miller indices describe the orientation of planes and directions in a crystal lattice, cf Appendix A). When a shear stress is applied along such a plane parallel to the slip direction, the stress required to initiate dislocation motion is the minimum possible. It is defined as the critical resolved shear stress (τ_{CRSS}).

The τ_{CRSS} for copper (FCC) is approximately 0.48 MPa, while for molybdenum (BCC) it is about 48 MPa. This difference of two orders of magnitude is attributed to the denser packing of FCC slip planes compared to BCC ones.

Indeed, comparing the atomic configuration of slip planes reported in 1.3, the atomic density of the (110) BCC plane is

$$\frac{n \ of \ atoms}{surface} = \frac{2}{a^2\sqrt{2}} \tag{1.2}$$

since there is an entire atom in the dashed area, plus four quarters of an atom. For the (111) FCC plane,

[2] $\varepsilon = \int_{l_0}^{l} \frac{dl}{l}$,with l_0 and l initial and actual specimen's lengths. As described by Ludwik [17], solving the integral $\varepsilon = \ln \frac{l}{l_0} = \ln(1 + \varepsilon_{eng})$, with ε_{eng} engineering strain, directly obtainable by a tension test.

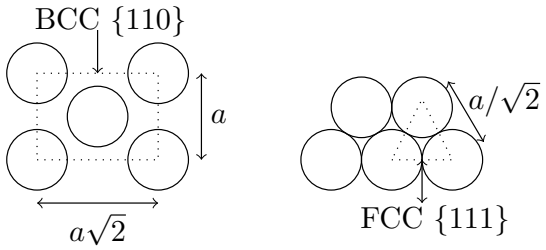

Figure 1.3: Atom configuration on a (110) BCC plane and on a (111) FCC plane (which is a close-packed plane).

the density is

$$\frac{n\ of\ atoms}{surface} = \frac{1}{\frac{\sqrt{3}}{4}\frac{a^2}{2}} = \frac{8}{\sqrt{3}a^2} \tag{1.3}$$

As there are three-thirds of atoms in the dashed area. For molybdenum (BCC) with lattice parameter $a = 3.15\,\text{Å}$, the resulting density is $14.3\,\text{nm}^{-2}$, while for copper (FCC) with $a = 3.615\,\mathring{A}$ the density is $35.3\,nm^{-2}$, more than twice that of Mo.

This resistance to dislocation motion arising from the crystal structure is known as the *Peierls stress,* τ_p, which can be expressed as:

$$\tau_p \simeq 2\mu\, exp\left(\frac{2\pi w}{b}\right) \tag{1.4}$$

Where μ is the shear modulus, defined as the ratio of shear stress to shear strain, w is the dislocation width, and b is the Burgers vector.

However, this contribution alone cannot explain the mechanical resistance of materials, since the theoretical τ_{CRSS} is much lower than the experimentally observed yield stress.

The Peierls stress previously described referred to a single crystal. While some engineering applications benefit from single-crystal materials (e.g., creep-resistant materials), most materials are not single crystals. Instead, they are polycrystalline, consisting of many individual grains. These grains originate during solidification, when different nuclei grow independently and impinge on each other, forming regions that share the same crystal lattice structure but differ in orientation. As a result, a polycrystal is a collection of misoriented domains, each with its own crystallographic alignment, yet all based on the same fundamental unit cell.

By way of example, Figure 1.4 reports an electron diffraction image of an aluminum alloy. All the grains have an FCC structure with the same a, but they are oriented differently. The code colors used in that image is reported to the right: the z-axis points out of the screen (towards the viewer) is chosen as reference, if a grain shows its face with respect to this axis, that is, a plan of the family 001, it will colored red, if a 110 planes, that expose an edge of the cube in the z-direction, it will colored green while the 111 planes, oriented such that a corner or vertex of the cube is in z direction, will be colored blue. All intermediate orientations are displayed as smooth gradations between these three primary colors. Grain boundaries are defined as the interfaces where the crystallographic orientation changes (misorientation) by more than a threshold value, typically set in the range of 10–15 (in Figure 1.4, the threshold is 10). The presence of grain boundaries in polycrystalline metals is one important contributor to their strength for two fundamental reasons. If a dislocation (for example, an edge dislocation as reported in 1.5) moving along the close-packed direction in one grain (grain A) does not easily pass to the adjacent grain (grain B) because the close-packed directions do not align (dotted line).

The other contribution arises from the fact that the shear stress will be randomly oriented with respect to slip planes and directions. To illustrate this, let us consider a cylindrical sample of cross-sectional area A subjected to an external stress F (figure 1.6). Let F_s denote the component of F along the slip direction in a generic crystallographic plane. The resultant shear stress (τ), acting on the plane, can be expressed as:

$$\tau = \frac{F_s}{A_{plane}} = \frac{Fcos\lambda}{\frac{A}{cos(\phi)}} = \frac{F}{A}cos(\lambda)cos(\phi) = \sigma cos(\lambda)cos(\phi) \tag{1.5}$$

The factor $cos(\lambda)cos(\phi)$ is called *Schmidt factor* and although it can ideally vary between 0 and 1, given that dislocations usually slide along slip planes, its maximum value is obtained when F lies on the plane

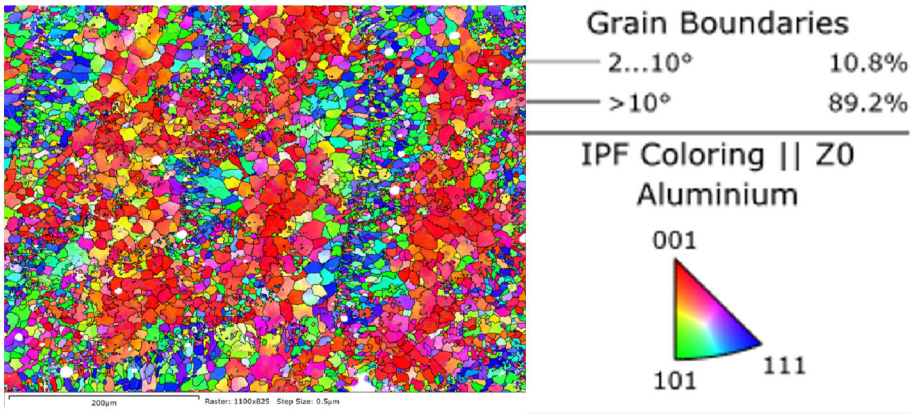

Figure 1.4: Electron diffraction image of an aluminum alloy showing individual grains, the code colors are reported to the right

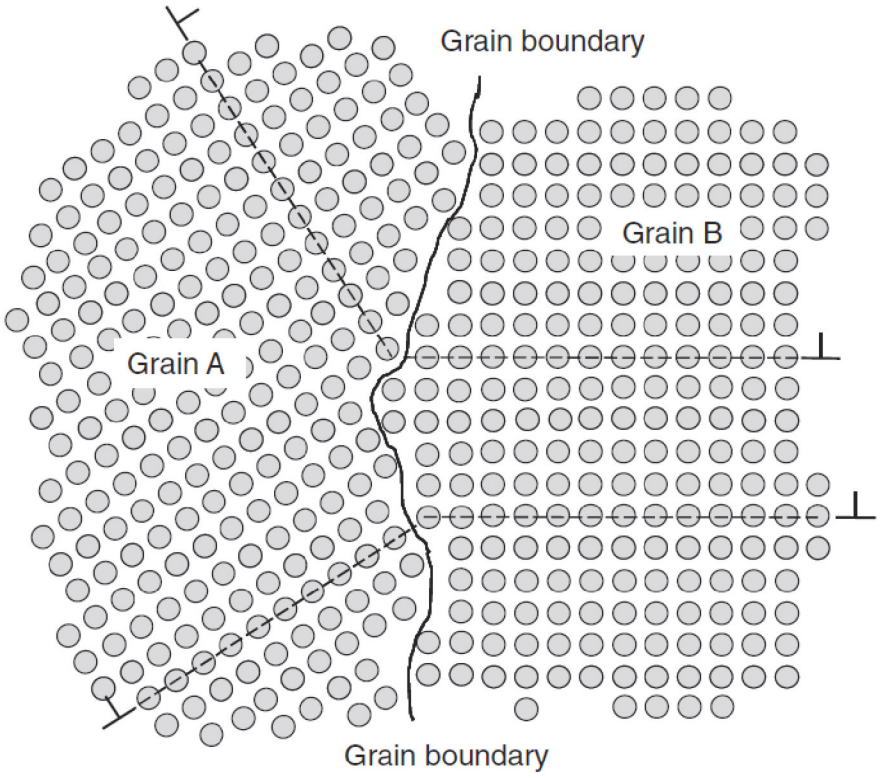

Figure 1.5: Schematic showing two simple cubic grains (which happen to align in a direction normal to the indicated plane) separated by a grain boundary. The close-packed direction of the two edge dislocations from grain A does not align with the close-packed direction in grain B.[22]

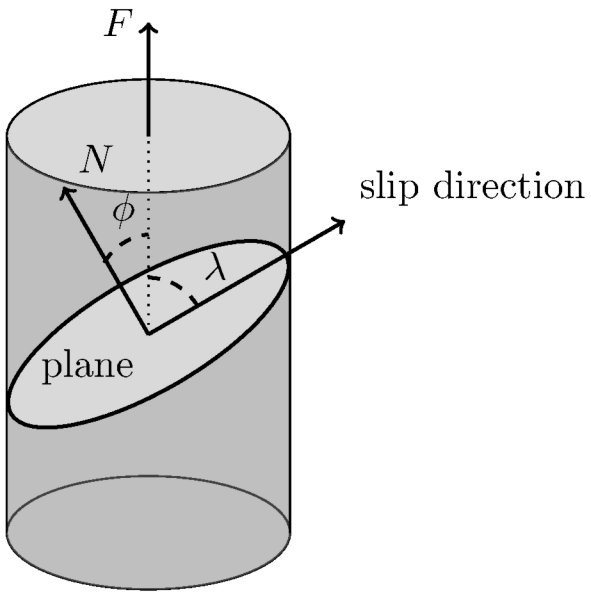

Figure 1.6: Slip plane, with normal N and direction with respect to external stress (F). The angle ϕ is the angle between F and N, while λ is the angle between F and the slip direction.

formed by N and slip direction, resulting in $\phi + \lambda = 90$ and therefore

$$(cos(\lambda)cos(\phi) = cos(\phi)cos(90 - \phi) = cos(\phi)sin(\phi) = \frac{1}{2}sin(2\phi) \tag{1.6}$$

resulting in a maximum value of 0.5 when $\phi = 45$.

Not every grains have got a *Schmidt factor* = 0.5, so the τ_{CRSS}, varies from grain to grain. Indeed, the initiation of yield in a few grains optimally oriented for slip does not imply bulk slip in the polycrystal; additional stress is required to compensate for the reduction caused by crystallographic orientation. *Widersich* [23] found the following relationship by studying the evolution of shear stress with increasing dislocation density (a concept known as strain hardening, which will be introduced in Section 1.1.2)

$$\tau = \tau_0 + A\mu b\sqrt{\rho} \tag{1.7}$$

with τ_0 the shear stress in a metal with low dislocation (e.g., annealed) and A a numerical constant, later defined as *geometrical factor*. Recalling (1.1), restricting the average distance moved by each dislocation to grain size (g_s), to maintain the same level of strain, given that b is constant, it must necessarily follow that

$$\rho \propto \frac{1}{g_s} \tag{1.8}$$

substituting in (1.7) the *Hall-Petch*[19] [20] equation is obtained:

$$\sigma = \sigma_0 + \frac{k}{\sqrt{g_s}} \tag{1.9}$$

where k is a constant accounting for A, μ and b.

Analyses of the factors governing the increase in a material's resistance to deformation initially considered the role of the crystal lattice itself, followed by the effect of crystallographic orientation, as quantified by the *Schmidt factor*. The framework was subsequently refined by incorporating the influence of grain boundaries, which serve as practical barriers to dislocation motion. In addition to these microstructural features, it is essential to note that metals are never completely pure. The presence of foreign atoms, whether intentionally introduced as alloying elements and precipitates or unintentionally retained as residual impurities, further enhances the strength through solid-solution strengthening mechanisms, whereby solute atoms hinder dislocation glide. Since these effects originate from atomic-scale imperfections, it is necessary to introduce the concept of point defects, which represent the fundamental building blocks of solid-solution strengthening.

From a thermodynamic perspective, at any temperature above absolute zero, thermal energy induces lattice vibrations (phonons). In the Maxwell-Boltzmann distribution, for any temperature $T > 0$, the

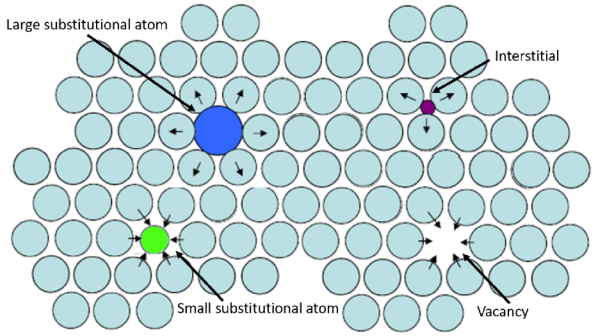

Figure 1.7: Impurity atoms added to a close-packed plane. Adapted from [22]

probability of a particle having an arbitrarily high (infinite) energy state is not zero but decays exponentially, approaching zero asymptotically. Thus, there exists a finite probability that an atom will acquire a displacement amplitude large enough to overcome the binding forces that keep it in its lattice site. The absence of such an atom creates a point defect (an imperfection of 1 atom, in contrast with line defects, dislocations) known as a vacancy.

Other types of point defects arise from the presence of foreign atoms. If this solute atom is sufficiently small, it can occupy an interstitial site in the lattice (the voids between the atoms of the crystal lattice). Conversely, if the solute atom replaces a host atom at a lattice site, the defect is referred to as substitutional. Both vacancies and solute atoms distort the periodic arrangement of the lattice: interstitial or oversized substitutional atoms generate local compressive stresses, while undersized substitutional atoms produce tensile stresses. These elastic distortions displace surrounding atoms from their equilibrium positions, perturbing the periodicity of close-packed planes (slip planes). Consequently, they act as obstacles to dislocation motion, thereby contributing to the strengthening of the crystal [24].

Fleischer [25] proposed a quantitative model in which the strengthening contribution of solutes is proportional to the square root of their concentration, reflecting the statistical nature of dislocation–solute interactions:

$$\Delta\sigma = \sigma_i + k\sqrt{c} \tag{1.10}$$

with σ_i stress without impurity atoms, c concentration of impurity atoms and k a constant.

1.1.2 Strain hardening

The *Widersich* equation (1.7) was initially introduced to illustrate the *Hall–Petch* relation between stress and grain size; however, the concept that dislocations themselves act as obstacles to the motion of other dislocations was not empathized. This phenomenon arises from the fact that each dislocation represents a distortion of the crystalline lattice, thereby interfering with slip along the crystal planes.

All the other strengthening mechanisms discussed in Section 1.1.1 are, in essence, independent of dislocation density. When deriving constitutive relations for the flow stress of a given material, these factors can therefore be treated as constant with respect to accumulated strain, strain rate, or temperature. Strain hardening, however, represents an exception, as it is by definition a function of strain.

Figure 1.8 shows a schematic stress–strain curve obtained for a well-annealed (low dislocation density) FCC single crystal, where shear stress is plotted as a function of shear strain. After the initial yield stress τ_1, associated with the critical resolved shear stress τ_{CRSS}, the curve enters a regime of *easy glide*, where dislocations generated during plastic deformation move freely through the single crystal without significant obstacles.

At a higher stress level τ_2, the strain hardening rate increases sharply (region II). Here, multiple slip systems become active, and the density of obstacles rises rapidly as dislocations interact and impede each other across different slip planes. The hardening rate remains constant in this regime, which is commonly referred to as stage II hardening. After this continuous rate, an equilibrium is reached between dislocation generation and *recovery*, a process detailed in the subsequent discussion. In a polycrystalline sample, stage I did not exist, as the random orientation of grains facilitates the initial slip on multiple slip planes, and region II may not exist or may be very short-lived.

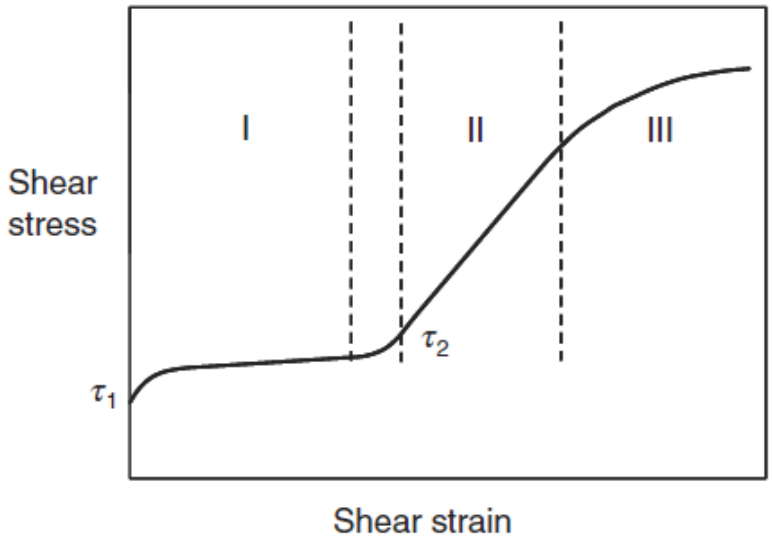

Figure 1.8: Stress–strain curve for a single crystal showing regions of easy glide, constant stage II hardening, and stage III, which is characterized by dislocation storage balanced by recovery, taken by [22].

The simplest model to describe a polycristalline sample strain hardening is a power law, firstly proposed by *Ludwik* in 1909 [17]

$$\sigma = \sigma_0 + K\,\varepsilon_p^n \tag{1.11}$$

where σ_0 is the yield stress, and K and n are material constants.

This simple law performs very well at low strain values; however, its limitation is that it doesn't saturate the stress at large strains. Indeed, its limit as the strain tends to infinity is infinite. In fact, an increase in applied stress enhances the probability that a dislocation will overcome the obstacles impeding its motion, a process known as "dynamic recovery".

A constitutive law that incorporates this effect with physically-based parameters is the Voce law [26]. This model introduces a saturation stress (σ_s), which is the stress value at which the rate of dislocation generation equals the rate of recovery, resulting in a zero rate of hardening.

$$\sigma = \sigma_s - (\sigma_s - \sigma_0)\exp\left(-\frac{\theta}{\sigma_s}\epsilon\right) \tag{1.12}$$

with θ the hardening rate, a material parameter function of strain rate and temperature.

This parameter has a physical meaning; it represents the constant $\frac{d\sigma}{d\varepsilon}$ rate of a single crystal (no dislocation obstacles deriving from grain boundaries) immediately after the "easy glide" region and before dynamic recovery starts, usually referred to as "stage II hardening rate" (Figure 1.8 [22]).

An equivalent formulation of the Voce equation, expressed by differentiating for ε

$$\frac{d\sigma}{d\epsilon} = \theta\left(1 - \frac{\sigma}{\sigma_s}\right) \tag{1.13}$$

It is a matter of fact that dislocation accumulation leads to strain hardening. However, as plastic deformation proceeds, the storage rate of dislocations progressively balances the rate of annihilation due to dynamic recovery. This results in a saturation of dislocation density ρ_d, and consequently, a saturation of flow stress. In other words, at sufficiently large strains, the material reaches a steady-state condition where

$$\frac{d\rho_d}{d\epsilon} = \dot{\rho}_{\text{gen}} - \dot{\rho}_{\text{rec}} = 0 \tag{1.14}$$

and the stress no longer increases with strain. The Voce equation (Eq. 1.12) captures this behaviour phenomenologically by introducing the saturation stress σ_s. Physically, this corresponds to the stress level at which the net rate of dislocation density evolution becomes zero.

At very high strain rates, the saturation stress tends to shift to higher values, as commented in 1.1.3.

The concept of a saturation stress (σ_s) in the Voce law arises naturally from the dynamic equilibrium reached between dislocation accumulation and dynamic recovery mechanisms during plastic deformation.

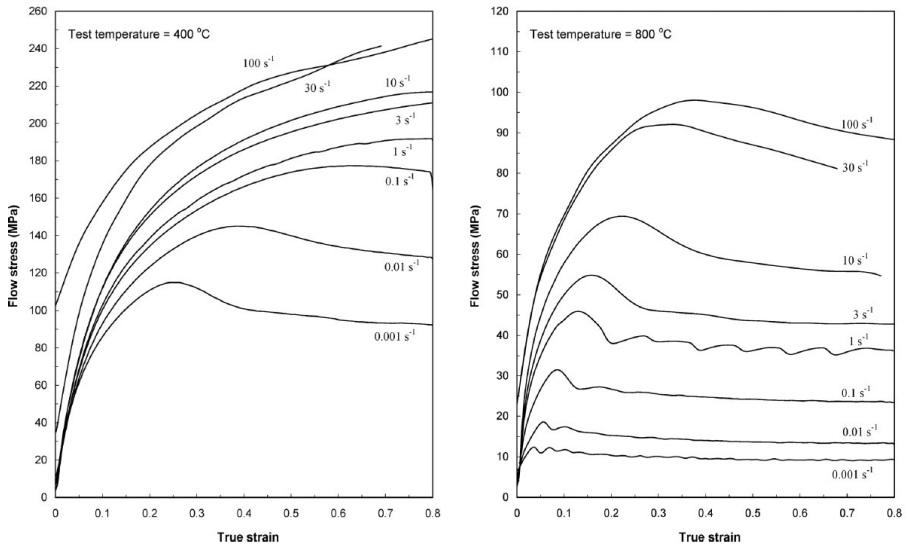

Figure 1.9: Effect of strain rate in an annealed copper sample at 400 °C and 800 °C [27].

As plastic strain progresses, the dislocation density ρ_d increases according to the Orowan relation (Eq. 1.1), leading to enhanced interactions between dislocations and obstacles such as other dislocations, solute atoms, precipitates, and grain boundaries. This results in an increasing resistance to dislocation motion, manifested macroscopically as strain hardening.

However, the accumulation of dislocations is counterbalanced by thermally activated processes that allow dislocations to annihilate, rearrange, or bypass obstacles. Mechanisms such as dislocation cross-slip, climb, and formation of subgrain structures facilitate recovery of the crystal lattice, thereby reducing the effective density of mobile dislocations contributing to further hardening. This dynamic equilibrium defines a saturation state, where the rate of dislocation generation equals the rate of recovery. In this regime, additional plastic strain does not significantly increase the flow stress, and the material exhibits a plateau in the stress–strain response.

Mathematically, the Voce law (Eq. 1.12) incorporates this behavior by introducing σ_s as a limiting stress, while the differential form (Eq. 1.13) expresses the evolution of hardening as a function of the instantaneous distance from saturation: the hardening rate $\frac{d\sigma}{d\epsilon}$ decreases progressively as the stress approaches σ_s. Physically, this reflects the reduced effectiveness of dislocation multiplication in the presence of increasing recovery events. The hardening rate θ represents the intrinsic ability of the crystal to resist plastic flow before recovery becomes significant, often corresponding to the "stage II hardening" observed in single crystals.

In practical terms, incorporating a saturation stress is essential for realistic constitutive modeling of metals subjected to large plastic strains, as it captures the transition from early-stage rapid hardening—dominated by dislocation multiplication and interactions—to the steady-state flow observed at high strains. Neglecting σ_s can lead to overestimation of strength at large deformations and poor prediction of phenomena such as necking, dynamic recrystallization, or post-yield flow localization, which are critically dependent on the balance between dislocation accumulation and recovery

1.1.3 Strain rate effects

The strain-rate effect denotes the increase in flow stress with increasing deformation rate. Figure 1.9 illustrates the strain rate effect observed in OFHC copper at two different test temperatures, as reported by Prasad and Rao [27]. An increase in strain rate results in a marked rise in flow stress across the entire strain range, indicating rate-sensitive plastic behavior. 1.9.

An empirical law describing this phenomenon can be expressed in the following form:

$$\sigma(\varepsilon) = C \ln \dot{\epsilon} \tag{1.15}$$

being C a material constant.

This section attempts to provide a physical explanation for the increase in stress required to propagate a dislocation and the observed logarithmic dependency of stress on strain rate.

At higher strain rates, the time available for thermally activated dislocation motion is reduced; therefore, additional stress is required to sustain plastic flow. Indeed, to overcome an obstacle, a dislocation must acquire sufficient energy, supplied either by the applied stress or by thermal fluctuations. The latter are governed by Boltzmann statistics, which state that atomic energies are not uniform but distributed statistically. As a result, a dislocation may spend a characteristic waiting time (Δt) before acquiring the necessary thermal energy, which can be expressed as:

$$\Delta t = \nu_0 \exp\left(\frac{\Delta G}{kT}\right) \tag{1.16}$$

where ν_0 is the attempt frequency (number of thermal fluctuations per second), ΔG is the Gibbs free energy barrier of the process, k is the Boltzmann constant, and T is the absolute temperature.

It follows that, if the deformation rate increases, the time available to a dislocation to "wait" for thermal energy is reduced. Therefore, thermal activation becomes less effective, requiring an increase in mechanical stress to overcome the obstacle. Recalling (1.1), dividing both member for Δt and substituting in (1.16)

$$\dot{\epsilon} = \rho_d b \frac{l}{\Delta t} = \rho_d b l \nu_0 \exp\left(-\frac{\Delta G}{kT}\right) = \dot{\epsilon}_0 \exp\left(-\frac{\Delta G}{kT}\right) \tag{1.17}$$

defining $\dot{\epsilon}_0 = \sigma_d b l \nu_0 \Delta G$ is function of applied stress.

To describe this dependency, Follansbee [22] considered the case of a moving dislocation interacting with an obstacle, idealized as another dislocation oriented perpendicular to its motion. The length of the dislocation segment involved in overcoming the obstacle can be approximated as the spacing to the next obstacle, l. According to *Peach* and *Koehler* [28], the force acting on this segment is $\sigma b l$. Since the dislocation must move over a distance equal to b, the mechanical work performed during this process is $\sigma b^2 l$. If the total activation energy associated with the dislocation–obstacle interaction is denoted as G, the effective activation energy is then reduced to $\Delta G = G - \sigma b^2 l$. Substituting this expression in (1.17) and resolving for stress

$$\dot{\epsilon} = \dot{\epsilon}_0 \exp\left(-\frac{G - \sigma b^2 l}{kT}\right), \quad \sigma = \frac{G}{b^2 l} + \frac{kT}{b^2 l} \ln \frac{\dot{\epsilon}}{\dot{\epsilon}_0} \tag{1.18}$$

The comparison between (1.15) and (1.18) highlights the limitations of the empirical law: although the constant C has a physical basis, it also exhibits a dependence on temperature T, which is not accounted for in the simplified model.

$$C = \frac{G - kTln(\dot{\varepsilon_0})}{b^2 l} \tag{1.19}$$

This temperature dependence of constant C is clearly visible in Figure 1.9: at the same level of true strain, the difference in flow stress between two strain rates varies with the test temperature.

The behavior of dislocations under high strain rates (typically $\dot{\epsilon} > 10^3$ s^{-1}) is fundamentally different from that observed under quasi-static conditions. At low strain rates, dislocation motion is primarily governed by thermally-activated processes: dislocations wait at obstacles until they gain sufficient thermal energy to overcome them. As strain rate increases, the waiting time becomes comparable to or shorter than the atomic vibration period, and dislocation motion becomes drag-controlled rather than thermally activated [29, 22].

In this regime, the dislocation velocity approaches a significant fraction of the shear wave speed c_s, and the applied stress must provide sufficient power to balance the viscous drag force acting on dislocations:

$$B v_d = \tau b \tag{1.20}$$

where B is the dislocation drag coefficient, v_d is the dislocation velocity, τ is the resolved shear stress and b the Burgers vector. As a result, the flow stress exhibits a stronger dependence on strain rate, deviating from the purely logarithmic behavior predicted by thermally activated models.

Moreover, the dislocation density ρ_d may evolve differently at very high rates: the rate of dislocation multiplication (e.g. via Frank–Read sources) can exceed the rate of dynamic recovery, leading to a much steeper initial strain hardening and a higher dislocation storage rate. This effect contributes to the rapid increase in flow stress observed in Split-Hopkinson Pressure Bar (SHPB) and plate-impact experiments.

Also, saturation stress is influenced by stress rate, since dynamic recovery mechanisms (such as cross-slip and climb) are thermally activated and cannot operate effectively within the reduced timescale of deformation. This explains the observed strain-rate hardening of metals: not only the instantaneous flow stress but also its saturation value increase with strain rate.

1.1.4 Thermal softening

As shown in Figure 1.9, when comparing two different temperatures at the same strain rate, it can be observed that the flow stress decreases with increasing temperature. This effect, known as thermal softening, occurs because the increase in local temperature enhances dislocation mobility, thereby reducing the flow stress. Higher thermal agitation brings atoms closer together, allowing dislocations to overcome obstacles more easily under a given applied stress. As the temperature increases, additional thermally activated mechanisms begin to contribute to deformation, such as enhanced dislocation glide or vacancy diffusion along grain boundaries — and, at sufficiently high temperatures, even bulk diffusion may become relevant. At this point, the deformation process gradually transitions into the creep regime, a distinct field of study that falls outside the scope of this thesis.

An increase in the sample temperature may occur either when the material operates in a high-temperature environment or as a result of plastic deformation. Indeed, a significant portion of the mechanical work performed on the material is irreversibly dissipated as heat. This phenomenon, often referred to as adiabatic heating, is particularly relevant at high strain rates, where the time available for heat conduction is limited and the process can be considered nearly adiabatic. The fraction of plastic work converted into heat is commonly described by the Taylor–Quinney coefficient β.

This parameter, typically ranging between 0.85 and 0.95 for metals, indicates the percentage of the plastic work that contributes to temperature rise. At the same time, the remaining fraction is stored as defects in the microstructure (e.g., dislocations). The instantaneous temperature increase can be estimated as:

$$\Delta T = \frac{\beta}{\rho c_p} \int \sigma d\epsilon_p \tag{1.21}$$

where ρ is the material density and c_p is the specific heat at constant pressure. This temperature rise leads to thermal softening, which reduces the flow stress and alters the material response, especially under adiabatic or near-adiabatic conditions. Johnson and Cook [30] proposed an empirical temperature-dependent term

$$\sigma(\varepsilon) = \left(\frac{T - T_r}{T_m - T_r} \right)^m \tag{1.22}$$

where T_r is a reference temperature, T_m is the melting temperature and m is a material constant. The meaning of T_r becomes clear when introducing their model in 1.2.1. In this model, T_r represents the temperature at which thermal softening is absent.

1.2 Constitutive laws

"These constitutive laws characterize the mechanical behaviour of the material and consist of a set of mathematical idealizations of their observed behaviour" [31].

Constitutive models relevant to metals under dynamic loading can be broadly categorized into two types: phenomenological and physically-based models.

Phenomenological models are empirically derived, relying on fitting experimental data to a set of mathematical functions with adjustable material constants. Examples include the Johnson-Cook (JC) model and the Arrhenius-type model. The JC model [30] is widely used due to its relative simplicity, few material constants obtainable from experimental data, and its widespread implementation in various commercial finite element simulation packages. It expresses the flow stress as a multiplicative decomposition of strain hardening, strain rate sensitivity, and thermal softening:

$$\sigma = (A + B\varepsilon^n) \left(1 + C \ln \frac{\dot{\varepsilon}}{\dot{\varepsilon}_0} \right) (1 - T^m), \tag{1.23}$$

where A, B, C, n, and m are material constants. The model is typically applied in impact and high-strain-rate simulations due to its robustness, but it lacks a physical basis.

Data-driven (Machine Learning-based) models are emerging approaches of this category, such as those utilizing Artificial Neural Networks, which are increasingly employed to capture highly complex and nonlinear relationships in material behavior, but suffer from the need for a large dataset to be trained. Therefore, their application was not feasible due to the limited data set available.

Physically-based models instead attempt to incorporate the fundamental underlying physical mechanisms of deformation, including, among others,

- Zerilli–Armstrong (ZA) model [32]: based on dislocation mechanics, it distinguishes between BCC and FCC metals. For example, for BCC metals, the constitutive law reads

$$\sigma = \sigma_a + B\varepsilon^n \exp\left[-(\alpha_0 - \alpha_1 \ln \dot{\varepsilon})\, T\right] \tag{1.24}$$

  where B and n are the hardening coefficient and exponent, $\alpha_0 0$ and α_1 are material constants which model the thermal and strain rate sensitivity, highlighting the role of thermal activation and dislocation density

- Mechanical Threshold Stress (MTS) model [33]: this model introduces the concept of a threshold stress $\hat{\sigma}$ that evolves with plastic strain and is thermally activated:

$$\sigma = \sigma_a + \frac{\mu(T)}{\mu_0}\left[s(\varepsilon_p, T, \dot{\varepsilon})\, \hat{\sigma}\right], \tag{1.25}$$

  where $\mu(T)$ is the temperature-dependent shear modulus and μ_0 is the shear modulus at $0\,K$. It is suitable for a wide range of strain rates and temperatures

- Preston–Tonks–Wallace (PTW) model [34]: developed for extreme strain rates (10^4–10^7 s^{-1}), such as those in shock loading, it accounts for dislocation drag and phonon interactions. Its general form can be expressed as

$$\sigma = \sigma_{th} + \sigma_{drag}, \tag{1.26}$$

  where σ_{th} is the thermal component and σ_{drag} represents the phonon drag-limited stress

- Molinari–Ravichandran (MR) model [35]: describes plastic deformation under high strain rates by explicitly coupling dislocation dynamics and thermal activation. It is particularly applied in adiabatic shear banding studies

The constitutive response of metals under dynamic loading is governed by the combined effects of strain hardening, strain-rate sensitivity, and thermal dependence, which act concurrently and often in competition with each other [22]. The interaction between these three mechanisms determines the overall constitutive response. Strain hardening and strain-rate strengthening increase the material's resistance to deformation, while thermal dependence acts in the opposite direction, reducing the strength and is therefore termed thermal softening. Accurate constitutive modelling under dynamic conditions must consequently account for the interplay between these mechanisms to correctly predict flow behaviour over a wide range of loading scenarios.

1.2.1 Johnson-Cook model

The Johnson-Cook (JC) model for flow stress is a product of three terms, describing strain hardening, strain rate, and temperature effects:

$$\sigma = (\sigma_0 + K\epsilon^n)\left[1 + C\ln\frac{\dot{\epsilon}}{\dot{\epsilon}_0}\right]\left[1 - \left(\frac{T - T_r}{T_m - T_r}\right)^m\right] \tag{1.27}$$

The strain hardening term is described by a power law, as shown in (1.11). The strain rate term and the temperature term are modified from the proposed (1.15) and (1.27) to ensure that the flow stress at reference strain rate ($\dot{\epsilon} = \dot{\epsilon}_0$) and reference temperature ($T = T_r$) is determined only by the strain hardening term.

The JK model, for instance, assumes a decoupled effect between strain hardening, strain rate, and thermal softening parameters. This fundamental assumption often leads to its failure in predicting flow behavior, particularly under large displacements, high strain rates, or high temperatures. A typical example of JK failure in predicting flow stress was provided by *Follansbee* in [36]. Two identical copper samples were strained to 0.15 at different strain rates, then unloaded and reloaded at the same strain rate. Although the two samples are composed of the same material and deformed to the same strain level, their mechanical response differs due to the different strain rates at which the first strain was imposed.

The JC model, like other phenomenological approaches, is formulated in terms of state variables, which are defined independently of the path taken to reach a given state. Strain, however, cannot be considered a state variable, since plastic deformation involves irreversible processes associated with energy dissipation and entropy production. As a result, the material response depends not only on the current state but also on the thermomechanical history of deformation, the path followed. For these reasons,

a physically-based model, the MTS, has been used to predict the metal behavior of the sample in this work. Meanwhile, JK was used in cases where the predicted deformations were contained, for example, in the impactor.

1.2.2 Mechanical Threshold Stress (MTS) model

The primary concept of the model is the distinction between two contributions made to overcoming a dislocation in the presence of an obstacle: stress and thermal activation. This isolated contribution of stress from the thermal activation will correspond to the stress required to overcome the obstacle in the absence of thermal activation; this is a hypothetical 0 K stress. It is defined *mechanical threshold stress* and denoted as $\hat{\sigma}$. Using this definition, (1.18) becomes:

$$\sigma = \hat{\sigma} + \frac{kT}{b^2 l} \ln \frac{\dot{\epsilon}}{\dot{\epsilon}_0} = \hat{\sigma}(1 + \frac{kT}{G} \ln \frac{\dot{\epsilon}}{\dot{\epsilon}_0}) \tag{1.28}$$

To account also for contributions to the stress where thermal activation is unable to assist the dislocation past these obstacles (e.g., grain boundaries, solution and precipitation hardening), *Follansbee* introduced an athermal stress component in (1.28). As stated in section 1.1.2, this term is generally considered independent of the accumulated strain, and this is therefore treated as a constant value.

$$\sigma = \sigma_a + \hat{\sigma} \left(1 + \frac{kT}{G} \ln \frac{\dot{\epsilon}}{\dot{\epsilon}_0} \right) \tag{1.29}$$

When analyzing the temperature dependence of the yield stress, it is important to separate the contribution from thermal activation from other temperature-dependent factors that are not directly related. In particular:

- The Burgers vector b does vary with temperature, but this change is negligible and can typically be ignored.
- The shear modulus μ, while its variation with temperature is small, should be explicitly removed from the equation, so that the remaining temperature dependence reflects only the contribution from thermally activated dislocation motion.

To do this, equation (1.29) can be rewritten as:

$$\sigma = \sigma_a + \frac{\mu}{\mu_0} \hat{\sigma} \left(1 + \frac{kT}{G} ln(\frac{\dot{\varepsilon}}{\dot{\varepsilon_0}}) \right) \tag{1.30}$$

with μ_0 shear modulus at 0 K. This temperature-dependent shear modulus μ can be expressed as

$$\mu = \mu_0 - \frac{b_1}{exp(\frac{b_2}{T} - 1)} \tag{1.31}$$

with b_1 and b_2 material constants. Also, the activation energy G carries a dependence on shear modulus; this can be factored out by introducing a normalized activation energy g_0, dividing G by μb^3, giving

$$\sigma = \sigma_a + \frac{\mu}{\mu_0} \hat{\sigma} \left(1 + \frac{kT}{g_0 \mu b^3} ln(\frac{\dot{\varepsilon}}{\dot{\varepsilon_0}}) \right) \tag{1.32}$$

Although strain (ϵ) is not a state variable, the athermal component of stress ($\hat{\sigma}$) is. Therefore, a convenient constitutive state-variable relation can be written as $\sigma = f(\hat{\sigma}, \dot{\epsilon}, T)$. An expression of this form was already provided in (1.28), although limited to the yield stress. What is needed, instead, is an equation of the type $\frac{d\sigma}{d\epsilon} = f(\hat{\sigma}, \dot{\epsilon}, T)$. This can be obtained by recalling the derivative form of the Voce equation presented in (1.13), now rewritten in terms of $\hat{\sigma}$.

$$\frac{d\hat{\sigma}}{d\epsilon} = \theta \left(1 - \frac{\hat{\sigma}}{\hat{\sigma}_s} \right) \tag{1.33}$$

The strain-rate dependence of θ has been empirically defined using an equation of the form

$$\theta = a_0 + a_1 ln(\dot{\varepsilon}) + a_2 \sqrt{\dot{\varepsilon}} \tag{1.34}$$

The temperature and strain rate dependency of the saturation stress at 0K ($\hat{\sigma_s}$) have been proposed by *Kocks*[29]:

$$\hat{\sigma}_s = \hat{\sigma}_{s0} \left(\frac{\dot{\epsilon}}{\dot{\epsilon}_{s0}} \right) \exp \left(\frac{T}{A_{CS}} \right) \tag{1.35}$$

with $A_{CS}, \dot{\epsilon}_{s0}$ and $\hat{\sigma}_{s0}$ material constants.

Kocks [29] provided a physically-based description of the strain-rate and temperature dependence of the mechanical threshold stress $\hat{\sigma}$. He postulated that the plastic flow rate $\dot{\epsilon}$ is governed by a thermally-activated process characterized by a normalized activation energy g:

$$\dot{\epsilon} = \dot{\epsilon}_0 \exp \left[-g(\hat{\sigma}, T) \right] \tag{1.36}$$

where $\dot{\epsilon}_0$ is a reference strain rate. The activation energy g is expressed as a function of the normalized stress $\hat{\sigma}/\hat{\sigma}_s$:

$$g = \left[1 - \left(\frac{\hat{\sigma}}{\hat{\sigma}_s} \right)^p \right]^q \tag{1.37}$$

Where p and q are material-specific constants describing the obstacle profile (rectangular, parabolic, or other shapes). Solving for $\hat{\sigma}$ leads to:

$$\hat{\sigma} = \hat{\sigma}_s \left[1 - \left(\frac{kT}{g_0 \mu b^3} \ln \frac{\dot{\epsilon}_0}{\dot{\epsilon}} \right)^{1/q} \right]^{1/p} \tag{1.38}$$

This relation demonstrates that $\hat{\sigma}$ increases with strain rate and decreases with temperature, consistent with experimental observations.

The derivation of the MTS requires calibrating numerous material constants:

- σ_a (MPa), the athermal stress component
- μ_0 (GPa), the shear modulus at 0 K
- $b_1(MPa)$ and b_2, material constants for the determination of μ(T)
- $\hat{\sigma}_{s0}$ (MPa) and $\dot{\varepsilon}_{s0}$ (s^{-1}) material constants for the determination of the saturation MTS
- g_0 normalized activation energy
- p and q, material constants describing the obstacle profile
- a_0, a_1 and a_2, material constants for the determination of the strain hardening θ;

Nevertheless, this law provides a theoretical model for understanding material behavior at high strain, strain rates, and temperatures. However, this theoretical understanding is only possible through mechanical testing, which is needed both to obtain data for calibrating the model's constants and to validate its conclusions.

1.3 Mechanical tests

Mechanical testing has a long and fascinating history. The earliest documented tensile experiments can be traced back to *Leonardo da Vinci*, who investigated the maximum load that iron wires could sustain as a function of their length. He observed that longer wires tended to fail under lower loads, intuitively linking this behavior to the higher likelihood of defects occurring along a greater length of material [37]. Over the centuries, these efforts evolved, leading to the development of modern testing machines in the 19th century. While tensile testing provides highly valuable information about material behavior, it will not be discussed in detail in this chapter, as an extensive and comprehensive body of literature already exists on the topic. The limitation in the maximum achievable strain rate ($\sim 10 s^{-1}$) has driven the development of testing methods capable of reaching higher strain rates.

1.3.1 Split-Hopkinson pressure bar

Hopkinson bar is named after the pioneering work of *J. Hopkinson*, who studied iron wire [38] and his son *B. Hopkinson* [39], but has been established in dynamic material testing based mainly on the theoretical and experimental work of *R.M. Davies* [40] and *H. Kolsky* [10]. In particular, the introduction of a second pressure bar (the output bar) by Kolsky led to the system known as the *Split Hopkinson*

Pressure Bar (SHPB) or *Kolsky* bar. Initially developed for high-strain-rate compression testing of small metallic specimens, the SHPB technique was later adapted to enable tension and torsion configurations. Its primary purpose is to determine the dynamic stress–strain response of materials by applying the elastic one-dimensional wave propagation theory to instrumented bars and analyzing the resulting strain histories.

The method consists of applying a tensile or compressive load to the specimen through a stress wave generated by the impact of a projectile on an apparatus comprising two identical, axially aligned bars (input and output), each instrumented with strain gauges. The specimen is positioned between the bars (Figure 1.10. The strain gauges mounted on the input bar record both the incident and reflected waves. Since the two bars have identical mechanical impedance, the reflected signal accounts for any additional reflections occurring at the specimen–output bar interface. The strain gauges on the output bar measure the transmitted wave, which is taken as directly proportional to the force transmitted through the specimen. This assumption is valid because the identical impedance of the bars minimizes reflections at the specimen–bar interface, provided that dynamic stress equilibrium is achieved.

Indeed, due to the relatively short length of the specimen, the time scale of the experiment is sufficient to allow multiple stress-wave reflections within the specimen before significant plastic deformation occurs. These repeated reflections homogenize the stress distribution, resulting in a nearly uniform stress state across the specimen's cross-section and along its length.

Both bars must remain within the purely elastic regime during the experiment, so that all inelastic deformation is confined to the specimen. This ensures that the stress–strain curve obtained from the data reduction accurately represents the material's real constitutive response under dynamic loading.

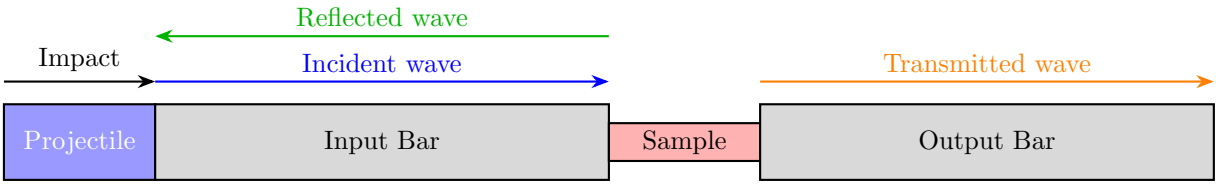

Figure 1.10: SHPB in compression.

To access even higher strain-rate regimes beyond the capabilities of SHPB techniques, impact-based methods are employed; however, these approaches come with intrinsic limitations that must be carefully considered.

1.3.2 Validation Role of High-Strain-Rate Impact Tests

Impact tests cannot provide a complete stress-strain response, yet they represent a fundamental tool for assessing the validity of constitutive models under extreme conditions. Unlike quasi-static or SHPB experiments, which primarily focus on well-controlled loading paths and provide detailed stress-strain data, impact tests expose the material to highly dynamic environments characterized by extreme strain rates, large plastic deformations, and significant adiabatic heating. These conditions often extend well beyond the experimental window of conventional techniques, thereby probing the material response in a regime closer to that encountered in real-world applications such as crash events, ballistic impacts, or blast loading.

In this context, the value of impact experiments lies in their indirect validation role. Instead of yielding continuous stress-strain curves, they provide measurable macroscopic outcomes, such as the final deformed shape of a specimen in Taylor or dynamic tensile extrusion tests, or the free-surface velocity histories captured in plate-impact and Richtmyer-Meshkov experiments. By comparing these experimental observables with numerical simulations based on constitutive parameters calibrated from quasi-static and SHPB data, it becomes possible to evaluate the predictive capability of the material model under conditions far removed from the calibration domain.

This cross-validation strategy ensures that the identified constitutive parameters are not limited to reproducing controlled laboratory curves, but also retain robustness when extrapolated to severe loading scenarios. As a result, impact tests serve as a crucial bridge between fundamental material characterization and realistic structural performance. They highlight the strengths and weaknesses of constitutive descriptions, guide the refinement of models, and ultimately contribute to establishing confidence in predictive simulations of dynamic events where safety, reliability, and performance are critical.

1.3.3 Taylor impact test

The Taylor impact test is an experimental method used to investigate the dynamic plastic deformation of materials under strain rates in the range of $10^2 - 10^4\,\mathrm{s}^{-}1$. Such high strain rates are achieved by accelerating a cylindrical specimen, typically using a gas gun or a drop-weight device, against a rigid target plate along its longitudinal axis. Upon impact, the specimen undergoes plastic deformation, resulting in the characteristic "mushrooming" of its frontal end, while the rear portion generally remains undeformed.

By measuring the final specimen geometry, such as the diameter of the mushroomed end, the length reduction, and the radial expansion, the deformation pattern can be compared with numerical simulations to validate the constitutive models. Unlike SHPB tests, Taylor impact tests do not provide a direct measurement of strain rate as a function of time, because the strain rate does not remain constant throughout the test duration. Instead, an approximate average strain rate can be estimated from the initial conditions of the experiment. Assuming that the specimen undergoes a predominantly homogeneous and uniaxial deformation during the early stages of impact (before the arrival of reflected waves from the free lateral surfaces), the average strain rate can be expressed as:

$$\dot{\epsilon} \approx \frac{v_0}{L_0} \tag{1.39}$$

where v_0 is the initial impact velocity of the specimen and L_0 is its initial length. This expression provides a first-order estimate of the strain rate, which is typically in the range of 10^2–$10^4\ \mathrm{s}^{-1}$. Numerical simulations can help to reconstruct a more accurate determination of the instantaneous strain rate profile vs time. However, for most experimental campaigns, the average strain rate is sufficient to classify the severity of the impact and to compare different tests under similar loading conditions.

1.3.4 Flyer-Plate tests

Plate impact tests, also known as flyer-plate or shock experiments, are widely used to investigate the response of materials under extreme strain rates (higher than those of Taylor impact), pressures, and shock loading conditions. In these tests, a flat projectile (the flyer plate) is accelerated to high velocities, typically using gas guns, explosive-driven techniques, electromagnetic launchers, or laser-driven systems, and impacts a target plate. The impact generates a nearly one-dimensional stress wave, or shock wave, that propagates through the material, inducing high strain rates ($10^4 - 10^7\mathrm{s}^{-1}$) and pressures (from tens of MPa up to several GPa).

Measurements in plate impact experiments typically include the particle velocity, stress, or pressure history from the free surface velocity, which is acquired from the rear surface of the target using high-speed diagnostics such as VISAR (Velocity Interferometer System for Any Reflector), PDV (Photonic Doppler Velocimetry), or embedded stress gauges. These data allow the determination of the Hugoniot relations, which describe the relationship between shock stress, particle velocity, and specific volume, providing essential input for constitutive models and hydrodynamic simulations.

Unlike SHPB or Taylor impact tests, which focus on plastic deformation at intermediate strain rates, plate impact tests explore the ultra-high strain-rate and shock regime, bridging the gap between conventional mechanical testing and extreme dynamic events such as ballistic impact or blast loading. Unfortunately, in addition to a high strain rate, this test exerts very high pressure.

High pressure causes pressure hardening, which can be quite problematic because it cannot be experimentally separated from strain rate hardening in the resulting material response.

In classical plasticity theory, particularly in the von Mises yield criterion, the effect of hydrostatic pressure on yielding is neglected. The von Mises yield function is expressed as

$$f(\boldsymbol{\sigma}) = \sqrt{\tfrac{3}{2}\,\mathbf{s} : \mathbf{s}} - \sigma_y = 0, \tag{1.40}$$

where

$$\mathbf{s} = \boldsymbol{\sigma} - \tfrac{1}{3}\,\mathrm{tr}(\boldsymbol{\sigma})\,\mathbf{I} \tag{1.41}$$

is the deviatoric stress tensor and σ_y is the yield stress.

Since only the deviatoric stress enters the formulation, the hydrostatic pressure term

$$p = \tfrac{1}{3}\,\mathrm{tr}(\boldsymbol{\sigma}) \tag{1.42}$$

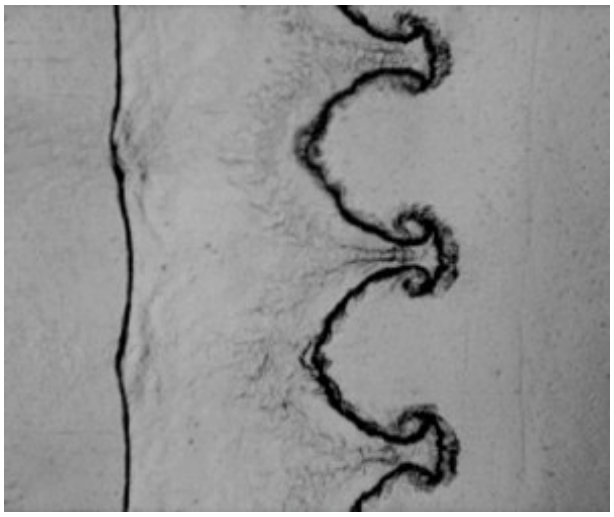

Figure 1.11: Richtmyer–Meshkov instability in fluids [42]

it does not affect yielding. However, in many metals and alloys under very high confining pressures, this assumption breaks down: materials exhibit pressure hardening, meaning their resistance to plastic flow increases with hydrostatic stress. This effect becomes particularly relevant in high-pressure applications, such as shock loading, dynamic compaction, and high-strain-rate deformation, where pressure-dependent yield models (e.g., Drucker-Prager or pressure-modified von Mises criteria) are more suitable.

In addition to pressure hardening, despite the high strain rate achievable with this test, the total strain attainable is relatively limited. For this reason, other tests have been conducted to achieve higher strain at the same strain rate and lower pressure.

1.3.5 Dynamic Tensile Extrusion (DTE)

Proposed by *Gray et al.* [13], the Dynamic Tensile Extrusion (DTE) test consists of a projectile launched at high velocity (typically by a gas gun or explosive driver) through a die with a calibrated hole, dynamically extruding the material. This test has proven effective in producing both very large plastic strains (exceeding 400% in annealed copper samples) and strain rates exceeding $10^5\,\mathrm{s}^{-1}$, while maintaining a relatively low shock pressure. Similarly to plate-impact tests, it is not possible to achieve a constant strain rate or a uniform stress state throughout the specimen. Consequently, a whole stress-strain curve cannot be directly obtained from this test. Nevertheless, the quantities measurable in a DTE experiment are extremely valuable for validating constitutive and damage models.

The interpretation of DTE results relies on numerical simulations that must be capable of capturing the evolving deformation and material flow. One of the significant challenges in modelling DTE is the accurate representation of the friction between the specimen and the die, which strongly affects flow behavior and strain localization. Uncertainties in the friction coefficient can lead to significant discrepancies between experimental observations and numerical predictions [41]. Furthermore, it is difficult to estimate the dependence of this coefficient on temperature T, strain rate $\dot{\epsilon}$, and stress state σ.

For this reason, alternative tests have been proposed to reproduce high strain rates and large plastic strains without the limitations imposed by simulating frictional wear.

One such approach is based on the Richtmyer-Meshkov instability (RMI), named after the researchers who first theoretically and experimentally investigated it. This method exploits a hydrodynamic instability which, under sufficiently intense loading conditions, can also occur in solid materials.

1.3.6 Richtmyer-Meshkov Instability (RMI)

The growth of irregularities at the interface between two fluids of different densities under gravity (Figure 1.11) was first theorized in the late 19^{th} century by Lord Rayleigh and later generalized by G. I. Taylor to encompass any accelerated motion. Richtmyer [43] incorporated the effects of compressibility and extended the theory to be valid also in cases of an abrupt change of acceleration (e.g., a shock wave). Indeed, in the incompressible formulation, the perturbation growth is assumed to be transmitted instantaneously through the pressure field, neglecting the finite propagation speed of acoustic waves.

Meshkov [44] experimentally confirmed Richtmyer's predictions by observing the growth of perturbations induced by a shock wave in a shock-tube setup. This phenomenon, now known as the Richtmyer–Meshkov instability (RMI), is fundamental in applications such as high-energy density physics problems, inertial confinement fusion, astrophysical flows, and even dynamic loading of solids, where similar interface instabilities can develop. (Figure 1.11)

Unlike tests such as DTE, where boundary conditions introduce modelling complexity (e.g., friction and confinement), RMI experiments often offer a cleaner interface-driven deformation scenario, making them particularly suitable for validating high-strain-rate

The acceleration of the flyer plate can be realized by several methodologies, such as:

- explosive-driven flyers, where a thin layer of high explosive is used to impart rapid acceleration through detonation, producing very high strain rates on the flyer surface,
- gas-gun techniques, that utilize a high-pressure gas to propel the flyer along a barrel, allowing precise control over velocity and impact timing,
- laser-driven flyers, that employ high-intensity laser pulses to ablate a material surface, generating thrust that launches the flyer at extreme velocities in a short time,
- electromagnetic (or railgun) accelerators exploit Lorentz forces to rapidly accelerate conductive flyers, offering fine tunability of velocity profiles.

The fundamental physical mechanism driving RMI is the baroclinic production of vorticity. A shock wave is passed through a disturbed interface between two fluids of different densities. This vorticity is generated at the perturbed interface due to the misalignment of the pressure gradient imposed by the shock wave and the density gradient (the two solids/fluids need to have different densities).

The geometric perturbation usually follows a sinusoidal law (Figure 1.12) with an initial amplitude η_0 and a wavelength λ.

$$x(y) = \eta_0 \cos(ky) \tag{1.43}$$

with $k = \frac{2\pi}{\lambda}$.

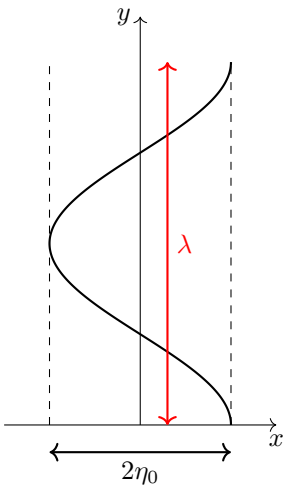

Figure 1.12: Representation of geometric perturbation, where λ is the wavelenght and $2\eta_0$ is the amplitude.

Richtmyer's equation (1.44) shows that the amplitude growth depends on gradient density (Atwood number $A = \frac{\rho_2 - \rho_1}{\rho_2 + \rho_1}$), the velocity jump imparted by the shock Δu and the geometric dimensionless parameter $\eta_0 k$

$$\dot{\eta} = \eta_0 k \, \Delta u \, A \tag{1.44}$$

The evolution of the Richtmyer–Meshkov instability can be qualitatively illustrated in Figure 1.13. This figure represents the sequence of events following the impact of a flyer on the sample, highlighting how the initial planar shock interacts with a sinusoidal perturbation at the interface and results in the characteristic formation of spikes and bubbles. In particular, at time t_0, the flyer impacts the sample, initiating the shock. By t_1, a single planar shock compression wave propagates through the material. At

t_2, the shock front reaches the beginning of the sinusoidal perturbation at the interface. By t_3, the wave has inverted locally in the regions where it has already interacted with the perturbation, while remaining in compression in the higher areas that the shock has not yet reached. This local inversion generates regions in compression and regions in tension, leading to a net material transfer from the compressive regions to the tensile areas, and resulting in the formation of spikes and bubbles, which are characteristic features of the Richtmyer-Meshkov instability.

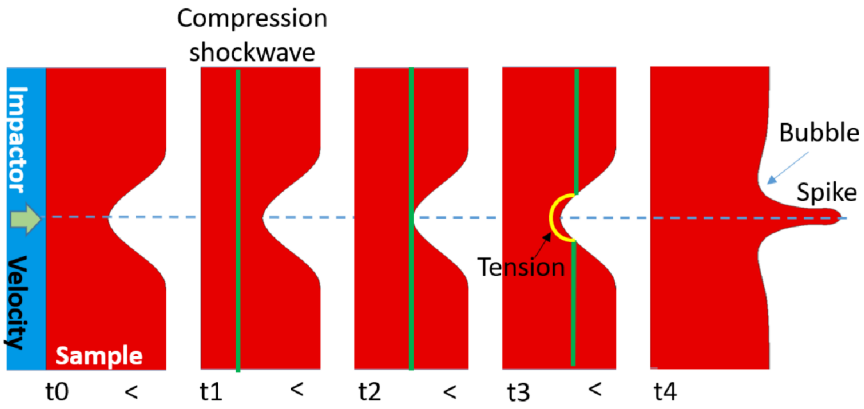

Figure 1.13: Schematic representation of RMI experiment

In the context of the Richtmyer–Meshkov instability, "bubbles" refer to the regions where the lighter fluid pushes into and displaces the heavier fluid. In comparison, "spikes" denote the areas where the heavier fluid intrudes into and displaces the lighter fluid. In our experiments, the light fluid is always air, maintained at a pressure below approximately 10 mPa (0.01 Pa), while the heavy fluid is copper. This leads to an Atwood number $A \approx -1$ and thus the perturbation will *invert*, with the generation of spikes.

Spike and bubble velocity can be measured experimentally by PDV, and their velocity (u_{sp}) is proportional to the strength of the material [45]. Piriz describes, in the case of $A = -1$, a relationship between spike velocity and material strength.

$$k(\eta_\infty - \eta_0) = 0.29(k\eta_0)^2 \frac{\rho u_{sp}^2}{Y} \tag{1.45}$$

with η_∞ amplitude at $t = \infty$ and Y yield strenght of the material.

Dimonte [46] finds that if the maximum of

$$\frac{\rho u_{sp}^2}{Y} < 10 \tag{1.46}$$

The perturbation will stop without the production of jet fragments.

Despite Richtmyer's equation (1.44) indicating that the growth rate of the amplitude is independent of the scale of the perturbation, Prime [47] shows that the strain rate is not. In particular, dividing both members by the initial perturbation amplitude, and ignoring the sign (with $A = -1$ the perturbation inverts):

$$\dot{\epsilon} \propto \frac{\eta_0 k}{\eta_0} \Delta u = k \Delta u = \frac{2\pi}{\lambda} \Delta u \tag{1.47}$$

So, the strain rate is inversely proportional to the perturbation wavelength. This leads to an advantage of RMI experiments for constitutive model validation, that is, their ability to essentially isolate the effects of strain rate on material strength from those of pressure. This is achieved, for instance, by designing targets with multiple perturbation regions of different length scales on a single sample, inducing varying strain rates while ensuring identical shock loading conditions, thereby isolating the strain rate as the primary variable.

Despite this, several perturbations of hundreds of microns in one sample can lead to several issues, such as the precision required in sample preparation (the mechanical preparation of the part plays a critical role) and the PDV spotlight dimension. In particular, the spot must be small enough to capture only one spike, resulting in a very difficult alignment of the PDV light and the possibility of measuring more than one spike in a single spot.

1.4 Thesis motivation

A significant, unresolved open question in the literature is which RMI experiments are suited to address the inconsistent observation of a substantial increase in strength (often referred to as a "strength upturn") at very high strain rates for ductile metals like copper. The question was addressed in a 2019 publication [48], where the authors attribute the phenomenon not to strain rate hardening but rather to a combined effect of pressure hardening and high temperature, which has not avoided criticism from other authors. In fact, since some authors claim to observe this phenomenon at a strain rate as low as $10^4\,s^{-1}$, other authors observed it at much higher strain rates. Some experimental studies and models predict this upturn, while others find no significant increase, highlighting a critical need for more robust and definitive validation methods to resolve these discrepancies.

In particular, Figure 1.14 reports a 3D graph that simultaneously shows the dependence of the flow stress on strain rate and pressure.

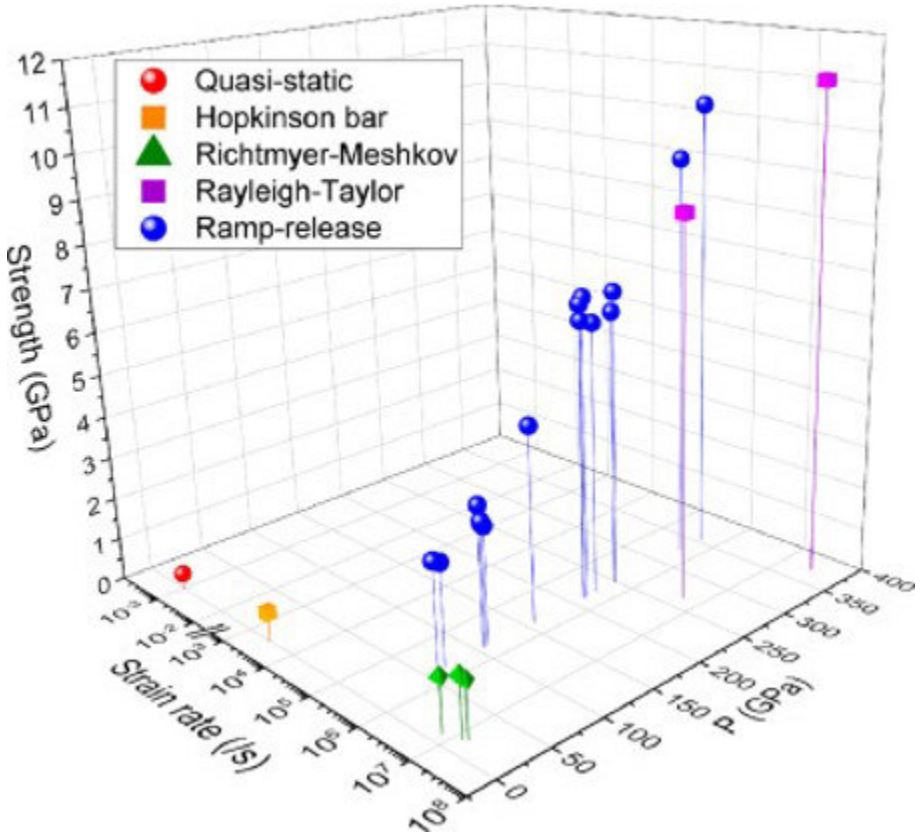

Figure 1.14: 3D graph that simultaneously shows the dependence of the flow stress on strain rate and pressure [49]

As can be seen, RMI can effectively obtain a high strain rate with relatively low pressure. To further reduce pressure, a simplified sample geometry will be proposed to achieve this.

- an improvement in the manufacturing quality and precision,
- improve the PDV measurement
- increases the volume of material involved in the deformation process
- a reduction in the planar impact-induced shock hardening

The proposed geometry features a single, central perturbation with a wavelength larger than those adopted in recent literature. The use of a gas-gun-propelled flyer ensures precise control over velocity, allowing several experiments to be performed by varying the perturbation wavelength and amplitude magnitude, while maintaining a constant pressure on the system.

Chapter 2

Experimental

2.1 Model validation

To assess the predictive capabilities of the MTS material model, the experiment published in 2024 by *Prime et al.* [47] was selected and numerically replicated as a benchmark. Velocity profiles were extracted from the numerical results and compared with those obtained experimentally, allowing for a quantitative evaluation of the model's accuracy. This validation provides a necessary foundation for applying the MTS model in the interpretation and design of forthcoming experimental investigations. Numerical simulations were performed using a commercial implicit multiphysics FEM code (MSC MARC r2022.3), which incorporates deformable bodies in contact. A total of 2k axially symmetric elements with four integration points was used as the initial mesh (Figure 2.1).

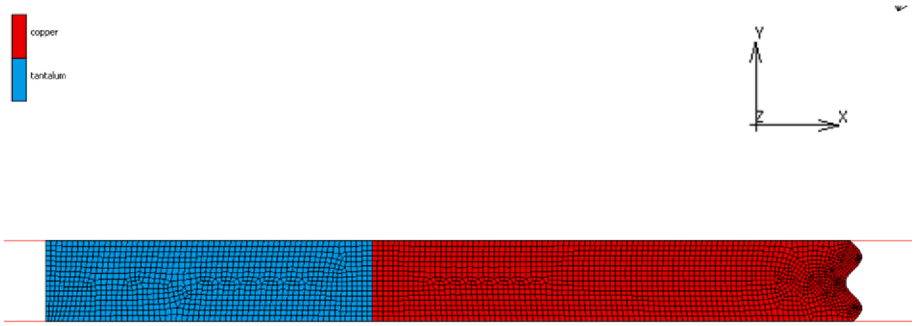

Figure 2.1: FEM model replicating Prime2024 experiments

A coupled thermo-mechanical analysis was conducted to account for thermal softening resulting from the conversion of plastic work into heat under quasi-adiabatic conditions. Simulations were performed under large displacement and finite strain formulation using the Lagrangian updating technique, while a single-step *Houbolt* procedure was chosen for the dynamic transient analysis. Lastly, global remeshing was employed to track material deformation.

Materials were modeled with elasto-plastic behavior; in particular, the impactor material (tantalum) was modeled with a simple stress-strain curve obtained at a strain rate of $3000\,\mathrm{s}^{-1}$ [50], meanwhile, copper dynamic behavior was reproduced with an MTS model calibrated with data published elsewhere [51]. Thus, to simulate jet fragmentation, a simple maximum plastic strain criterion was used. In particular, elements are removed when the average total equivalent plastic strain over the element Gauss points exceeds 700%. This limit value was selected to avoid nonphysical deformation due to remeshing of the necked ligament between the forming fragments. To the tantalum flyer, an initial velocity of 976 ms^{-1} was applied, as reported by *Prime et al.* A minimum of ten sample points was placed in the spike and bubble areas, respectively, to extract the x velocity versus time and calculate the average. The results for the $\eta_0 k = 0.9$ and $\lambda = 320\,\mu m$ experiment of *Prime* are reported in Figure 2.2 and compared with experimental data.

Time is plotted with reference to the onset of the loading. The model accurately captures the shape and amplitude of the velocity profile, reproducing the key features of the experimental response and validating its suitability for predictive use. Moreover, it is possible to extract the pressure at the free surface produced by the impact, as reported in Figure 2.3. The maximum difference between experimental

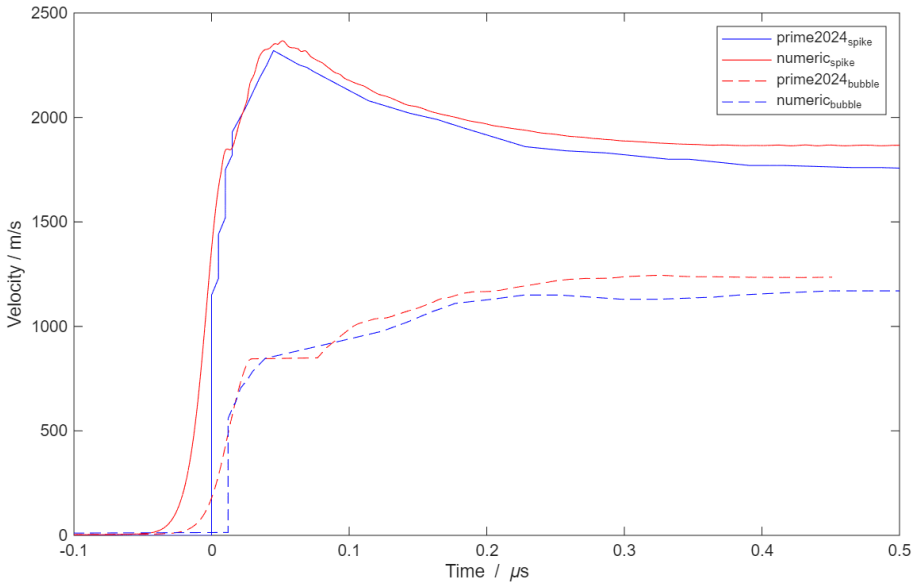

Figure 2.2: Comparison between experimental (Prime2024) and simulation

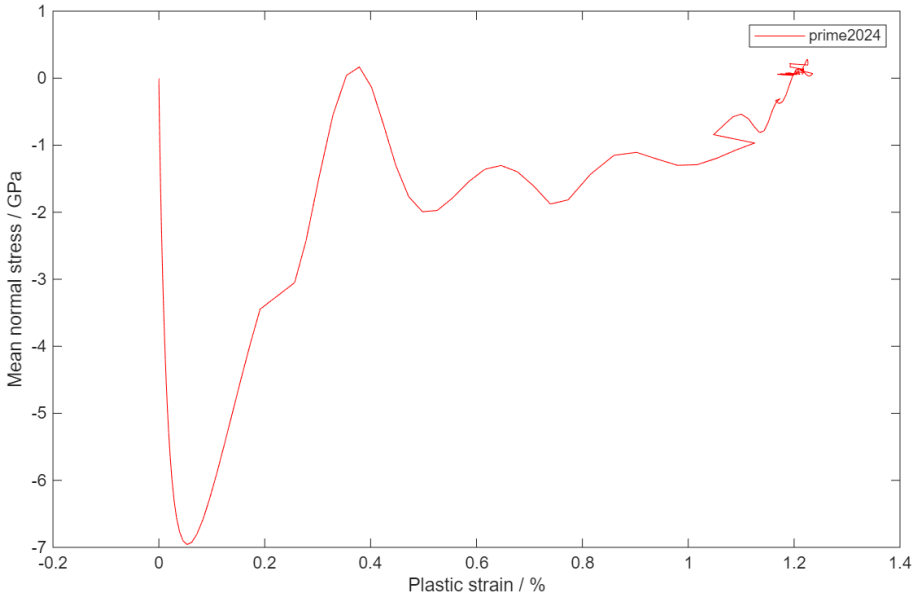

Figure 2.3: Mean normal stress and plastic strain at free surface

and numerical results was $-6\,\%$ for the spike and $-10\,\%$ for the bubble. The most likely cause of this discrepancy stems from the fact that the MTS model was calibrated using data obtained from an annealed copper specimen tested at the University of Cassino [51], rather than from the annealed copper data reported by Prime [47]. A less probable cause may be related to the absence of an Equation of State (EOS) for copper in the simulations. However, for such modest pressure levels, the corresponding density variation, according to the data reported by *Carpenter* [52], remains below $1\,\%$.

2.2 Preliminar numerical simulations

To design the most suitable geometries for the real specimen, a series of numerical simulations was conducted. The main objective was to reduce the overall pressure while increasing the size of the generated spikes, without altering the total strain. Although the strain rate naturally varies with the perturbation size, decreasing as the perturbation widens, the goal was to maintain it within a target range above $10^6\,\mathrm{s}^{-1}$. The idea behind this approach is to identify a configuration that can ensure both a measurable PDV signal and a deformation regime representative of the high-strain-rate domain. To design the most suitable geometries for the real sample, a series of simulations was carried out. The underlying idea was to reduce the pressure and increase the size of the spikes, while keeping the total strain constant. Although

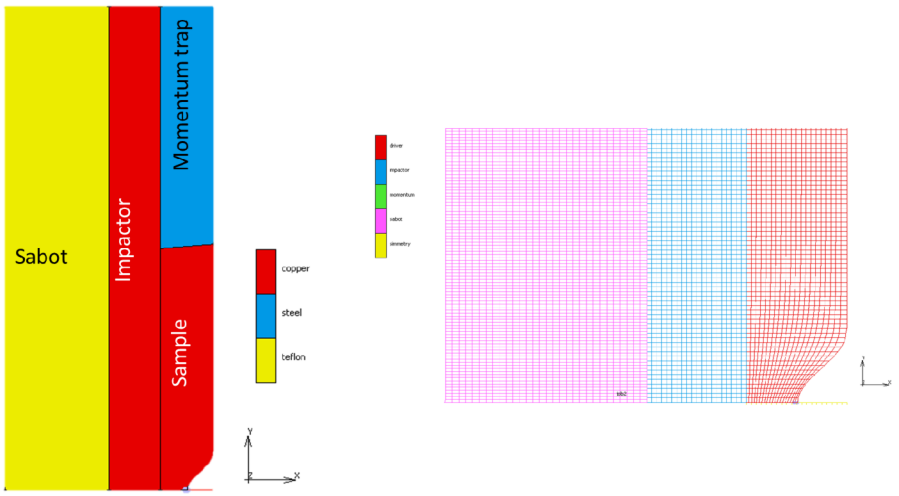

Figure 2.4: a FEM model example (Geometry2); on the left, a diagram of the simulated test components, on the right a magnification of the perturbation zone

the strain rate varies with the perturbation size (and thus tends to decrease), the goal was to remain within a target range higher than $10^6\,\mathrm{s}^{-1}$. Table 2.1 summarizes the simulated test configurations, where η_0 and λ represent the perturbation amplitude and wavelength, respectively (cf. Figure 1.12).

Table 2.1: List of simulated tests.

Geometry ID	η_0 (mm)	λ (mm)	$\eta_0 k$
1	0.25	1.6	0.98
2	0.5	3.2	0.98
3	1	6.4	0.98
4	0.125	1.6	0.49
5	0.25	3.2	0.49
6	0.5	6.4	0.49
7	0.5	1.6	1.96
8	1.0	3.2	1.96
9	2.0	6.4	1.96
10	2.5	16.0	0.98
11	5.0	32.0	0.98

The numerical simulation was performed using the same FEM code reported in section 2.1, employing an axial symmetry (x-axis) and deformable bodies in contact (left in Figure 2.4). The simulated bodies were the sabot, the impactor, the sample, and the momentum trap, a perforated disc that prevents reflected waves along the y-direction from interfering with the sample. A total of 17,000 axisymmetric elements with four integration points were used. The materials considered (polytetrafluoroethylene, steel, and copper) were modeled with elastoplastic behavior. In particular, a Johnson-Cook (JC) model was used for polytetrafluoroethylene and steel, accounting for both strain rate effects and thermal softening: The parameters used are reported in Table 2.2.

Table 2.2: Johnson-Cook (JC) parameters used for polytetrafluoroethylene and steel.

JC parameters	polytetrafluoroethylene	Steel
A (MPa)	75.8	1539
B (MPa)	68.9	477
n	1.85	0.18
C	0	0.012
m	1.85	1
$\dot{\varepsilon}_{p0}$	1	1
T_0 (K)	298	298

Copper, on the other hand, was simulated using the MTS model reported in section 2.1.

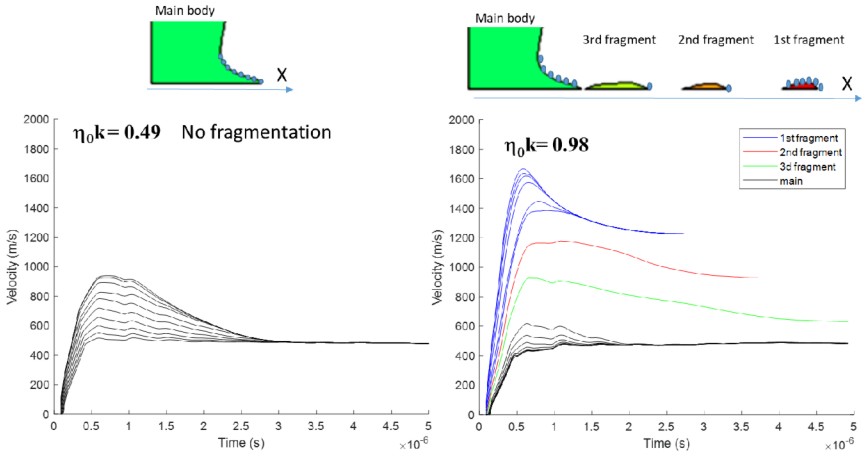

Figure 2.5: Velocity profiles in the event of insufficient $\eta_0 k$ (left) or sufficient $\eta_0 k$ (right) to cause fragmentation

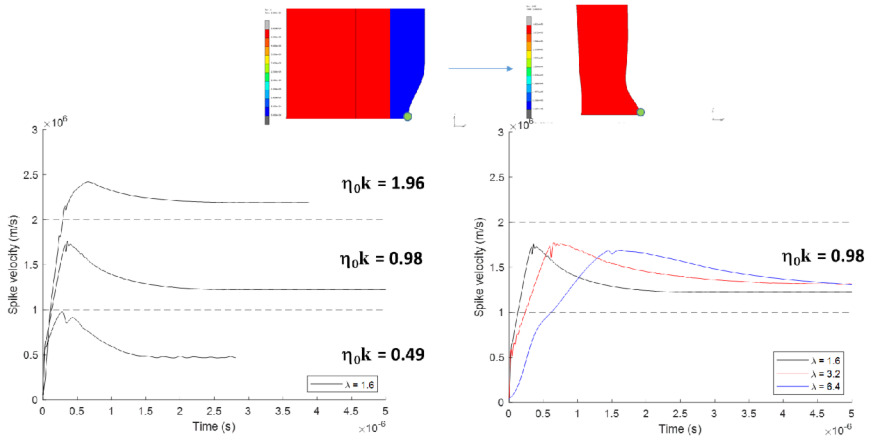

Figure 2.6: Comparison with a single sample point (top) from experiments at different values of $\eta_0 k$ (left) and comparison of the same value of $\eta_0 k$ but different values of λ (right).

The same analysis described in Section 2.1 was performed, using a coupled thermo-mechanical approach with global remeshing. A nodal velocity of $u = 500\,\mathrm{ms}^{-1}$ was applied to the sabot and impactor nodes for all tests; this value is realistically achievable with the available light gas gun.

By comparing the velocity profiles extracted from various sample points on the surface with the perturbation, in the case of $\eta_0 k$ not sufficient to induce fragmentation (left in Figure 2.5), it can be observed that during the first 2 μs there is an increase in velocity relative to u, followed by a convergence towards the initial velocity value ($500\,\mathrm{ms}^{-1}$). In the case of a $\eta_0 k$ value sufficient to cause fragmentation, it can be noted that the sample points located on the surface of the main body behave in a manner entirely analogous to what was observed previously (right in Figure 2.5), whereas those located in regions that will undergo fragmentation, after an initial velocity peak, tend toward an equilibrium velocity higher than the initial value.

Based on the previous observations, by selecting a single sample point at the location of maximum velocity (the intersection of the perturbation with the x-axis, top in Figure 2.6), it is possible to compare experiments conducted at different values of $\eta_0 k$. As shown on the left in Figure 2.6, increasing $\eta_0 k$ leads to both a higher peak velocity, reached around 0.5 μs, and a higher equilibrium velocity, reached after 1.5 μs.

Keeping $\eta_0 k$ constant while varying λ produces the results shown on the right in Figure 2.6. It can be observed that similar peak and equilibrium velocities are obtained. Still, with different time constants: for the specimen with $\lambda = 1.6$ mm, the peak velocity is reached within the first 0.5 μs, whereas for the specimen with $\lambda = 6.4$ mm, 1.5 μs are required.

For the same amount of strain, since the strain rate is the ratio of strain over time, different strain rates are obtained. To demonstrate this, a value of $\eta_0 k = 0.98$ was set, sufficient to trigger the perturbation instability (fragmentation), and a sample point was placed near the necking that occurred during the

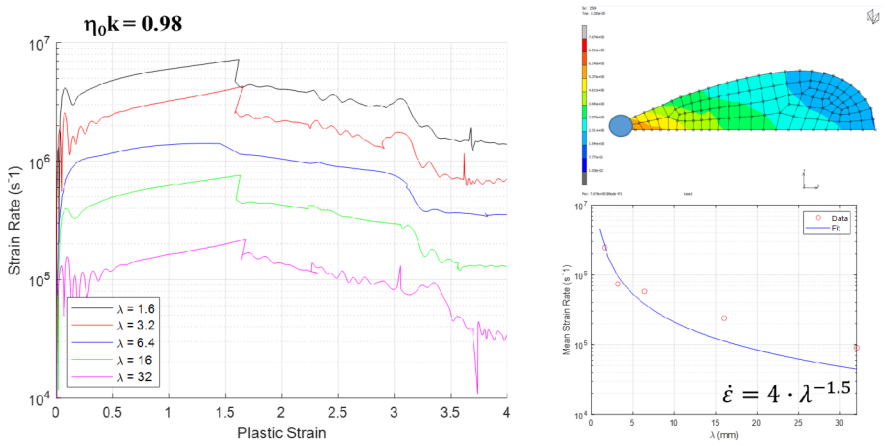

Figure 2.7: On the left, strain rate as a function of perturbation length λ, top right sample point used for analysis, and bottom right fit of average strain rate trend on λ

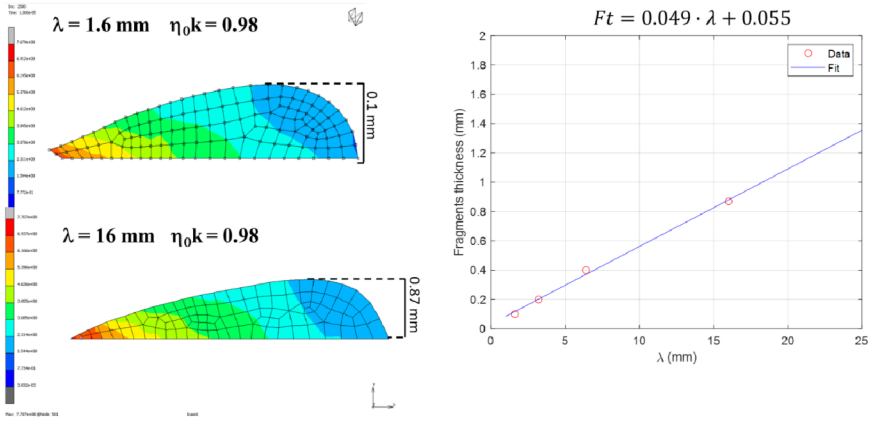

Figure 2.8: Thickness trend of fragments as a function of the value of λ

first fragmentation (top right in Figure 2.7).

The evolution of the strain rate as a function of plastic strain (left in Figure 2.7) is qualitatively similar when varying λ, i.e., it increases up to a plastic strain of about 1.5 and then starts to decrease; however, the absolute values gradually decrease as λ increases. A fit of the average strain rate values versus λ is shown at the bottom right in Figure 2.7.

Figure 2.8 shows instead that the fragment thickness relative to the perturbation width exhibits a linear trend.

The stress triaxiality (ST) is defined as the ratio between the mean stress (σ_m) and the von Mises equivalent stress (σ_{eq}):

$$ST = \frac{\sigma_m}{\sigma_{\text{eq}}} = \frac{\frac{1}{3}(\sigma_1 + \sigma_2 + \sigma_3)}{\sqrt{\frac{(\sigma_1-\sigma_2)^2+(\sigma_2-\sigma_3)^2+(\sigma_3-\sigma_1)^2}{2}}} \tag{2.1}$$

ST was measured at the necking point indicated by the blue arrow in Figure 2.9 and is reported as a function of plastic strain.

The overall trend of the ST with respect to plastic strain is reported in Figure 2.9; After a peak at highly negative triaxiality due to the impact, the triaxiality tends to converge towards a value of 0.3, which is typical for a uniaxial tensile test, if a few peaks, caused by ongoing issues with remeshing, are ignored.

2.3 Experimental Setup

2.3.1 Overview of the experimental challenge

The quantitative study of RMI in solid materials under high-strain-rate conditions necessitates a specialized experimental platform. Experiments utilizing gas guns or similar projectile launch systems generate the requisite shock pressures but introduce the challenge of managing the projectile's residual kinetic

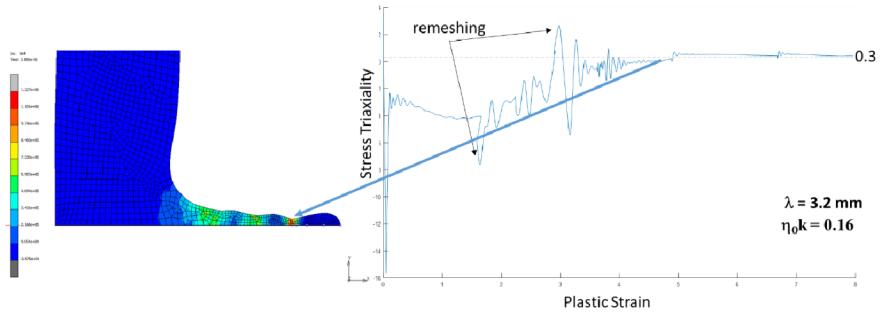

Figure 2.9: Stress triaxiality in function of plastic strain at the necking point (sample point indicated by blue arrow).

energy post-impact. Uncontrolled projectile motion can severely compromise the deformation of the specimen and interfere with sensitive diagnostic equipment. The design objective was to develop a system capable of isolating the specimen's deformation from the projectile's dynamics, thereby ensuring free surface motion, while simultaneously providing a stable platform for diagnostics such as PDV. The design and validation of this system, detailed in the following subsections, were guided by FEM simulations.

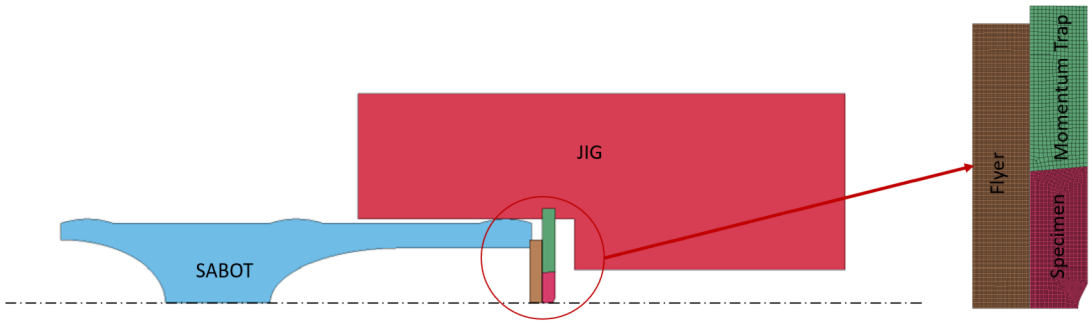

Figure 2.10: Schematic of the experimental setup for Richtmyer-Meshkov instability studies. Key components include the Sabot, Projectile, Specimen, Jig, and Momentum Trap, with the inset illustrating the meshing utilized in the FEM simulations.

2.3.2 System components

The experimental setup, illustrated in Figure 2.10, comprises three primary functional components: the projectile delivery system, the specimen, and the structural support/jig. Some changes have been made to the material compared to the initial simulations, and these will be detailed below.

The experiment is initiated by a projectile made of copper, launched by a gas gun, and housed within a sabot (made of polyamide) for guidance and sealing. The projectile is designed to impart a planar shock wave into the specimen (in copper), which typically features a pre-machined wavy interface to seed the RMI. The sabot incorporates a hollow geometry to mitigate the reflected pressure wave returning to the specimen. The interaction velocity and projectile geometry are selected to achieve the desired shock conditions (pressure and duration) necessary for instability growth. The integrity of this impact interface is critical, demanding precise alignment and flatness between the projectile and the specimen. A polycarbonate momentum trap is used to prevent the return of reflected waves along the y-axis. The specimen is held within this hollow ring using an interference fit, which ensures lateral stability and provides necessary support before impact. A tight tolerance of $\pm 0.05\,\text{mm}$ is maintained to secure the specimen while minimizing the induction of internal compressive stress. Initially, the design specifications derived from the preliminary FEM analysis (as detailed in Section 2.2) favored a carbon steel construction for the momentum trap, owing to its high yield strength and predictable energy absorption characteristics. However, this material choice was subsequently revised due to a combination of practical constraints. The high precision required for the internal surfaces presented significant mechanical realization challenges when working with steel. Furthermore, the high machining costs associated with the initial steel design prompted an intermediate investigation into more accessible materials. An attempt was made to utilize PLA (PolyLactic Acid) via additive manufacturing for preliminary tests; however,

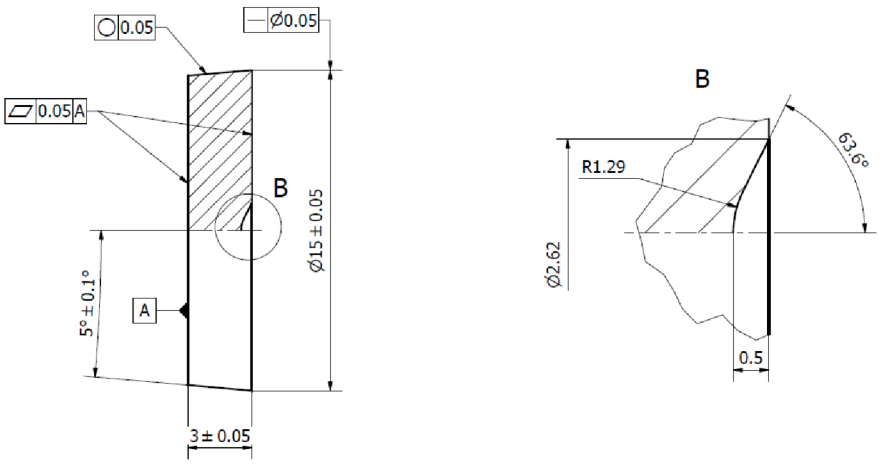

Figure 2.11: Example of specimen geometry

simulations confirmed that the polymer's low density and mechanical properties were entirely inadequate for reliably dissipating the kinetic energy of projectiles. Consequently, the final material choice settled on 3D printed polycarbonate, with a lower fabrication cost compared to the high-tolerance steel option, thereby ensuring both technical viability and budgetary efficiency (the momentum trap can be fabricated directly in the laboratory). The entire target assembly is held by a rigid structural component, labeled jig in figure 2.10. The jig provides the necessary stability to withstand the high forces generated upon impact. Furthermore, the jig serves as support for the PDV system. The operational demands placed on the energy dissipation system and wave reflection management necessitated validation through FEM simulations. The inset in Figure 2.10 demonstrates the meshing strategy used for the flyer, specimen, and momentum trap. These simulations were instrumental in:

1. dimensioning and material selection: optimizing the geometry and material choice of the jig and the momentum trap
2. stress and integrity analysis: assessing the structural response of the jig and other components to ensure they maintain integrity and alignment during the high-stress impact event.
3. decoupling verification: numerically confirming that the design successfully prevents the projectile's continued motion from imposing mechanical constraints on the specimen's rear surface, thereby validating the assumption of free surface deformation
4. wave management: simulations confirmed that no reflections returned to the specimen with sufficient capability to reach its free surface before the separation between the specimen and the flyer occurred.

The reliance on FEM before physical construction significantly optimized the design process, ensuring the experimental setup is robust and reliable.

2.4 Updated numerical simulations

For practical manufacturing reasons related to machining constraints, the specimen geometry was optimized to facilitate efficient machining. Instead of a fully cosine-shaped perturbation, the final configuration consists of a conical-like profile characterized by a single radius of curvature (cf. figure 2.11). This modification enables easier and more accurate fabrication in the mechanical workshop while preserving the essential features of the original geometry. No substantial difference emerged compared to the results presented in section 2.2. Two geometries, namely geometry 5 and geometry 8, were selected for the experiments. These geometries have different values of $\eta_0 k$ and were chosen because one promotes jet formation (8) and fragmentation, whereas the other (5) does not.

Before conducting the actual experiments, another parameter — the Zener–Hollomon parameter (Z) — was used to characterize these two geometries. This parameter is commonly employed to describe non-isothermal deformation under non-constant strain rate conditions:

$$Z = \dot{\varepsilon} \cdot e^{Q/RT} \tag{2.2}$$

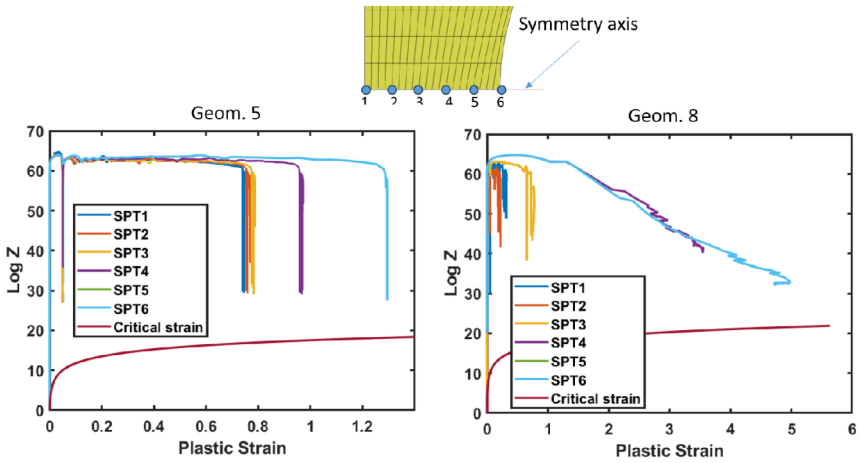

Figure 2.12: Sample points (left) and $\log(Z)$ trends as a function of plastic deformation.

where R is the ideal gas constant and Q is the apparent activation energy of the deformation process (similar to ΔG reported in Section 1.1.3). The temperature-dependent Q for copper was taken from the literature [53].

The evolution of $\log(Z)$ as a function of plastic strain was calculated for six sample points; these points and the $\log(Z)$ curves as a function of plastic strain are shown in Figure 2.12. As can be observed, all trends fall on the same curve, indicating that the deformation history is the same for all points in the specimen or, in other words, that the deformation at a material point is influenced more by temperature and strain rate than by its specific position in the sample. This implies that a single test can be performed, and different points of a fragment can be analyzed to collect data with interrupted deformation histories at a given strain value.

The parameter Z can also be used to estimate whether dynamic recrystallization (DRX) occurs. Dynamic recrystallization takes place when a critical strain ε_{cr} is reached, and the deformed grains tend to rearrange into new grains with a lower dislocation density. This strain, which is material-dependent, also varies with temperature, strain rate, and the initial grain size (g_s):

$$\varepsilon_{cr} = k_\varepsilon(g_s), Z(T, \dot{\varepsilon})^m \tag{2.3}$$

with m a material parameter and k_ε is usually expressed as a power law; however, it increases rapidly for smaller initial grain sizes and eventually reaches saturation for large ones [54]. For this reason, Hornqvist et al. [53] suggested that a Voce-type law provides a much better description of the evolution of the constant:

$$k_\varepsilon = \bar{k}_\varepsilon \left[(1 - \exp\left(-\frac{g_s^*}{g_s} \right) \right] \tag{2.4}$$

where g_s^* and $\bar{k}_\varepsilon$ are material constants. Critical strains have been added in Figure 2.12; no $\log(Z)$ curve intersects the critical strain, meaning that no DRX is expected to occur in the experiment.

To intentionally decrease the mean normal stress while maintaining significant plastic deformation, two simulations were performed using Geometry 8 at impact velocities of $400\,\mathrm{ms}^{-1}$ and $200\,\mathrm{ms}^{-1}$. The results were compared with the reference configuration discussed in [47] to evaluate the relative trends. Geometry 8 was chosen because it represents the most severe configuration, having the highest tested value of $\eta_0 k$, being the only configuration tested that leads to spike formation.

At $400\,\mathrm{ms}^{-1}$ (Figure 2.13, the maximum hydrostatic pressure was successfully reduced from about -7 GPa to -6 GPa. Although the strain rate decreased by approximately one order of magnitude, the plastic deformation evolved over a much broader range, extending up to 4% of plastic strain, compared to the 0.5% observed in the reference case. This behavior is consistent with our objective of promoting more distributed plastic flow under milder compressive conditions.

Further decreasing the impact velocity to 200 ms^{-1} (Figure 2.14) led to a maximum pressure of only -1 GPa, while still achieving strain rates on the order of 10^6 s^{-1}. This configuration, therefore, provides a favorable balance between a substantial amount of plastic deformation and a markedly reduced hydrostatic pressure.

Overall, the reduction of the mean normal stress proved effective in broadening the plastic strain distribution and mitigating the compressive state without excessively compromising the strain rate. These

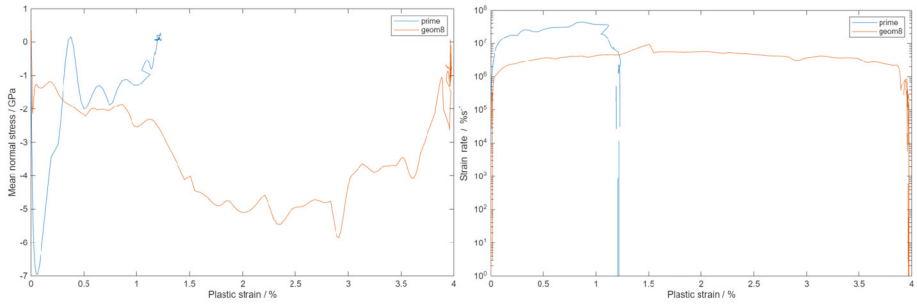

Figure 2.13: Mean normal pressure for Geometry 8 at $400\,ms^{-1}$ compared with Prime2024 experiments

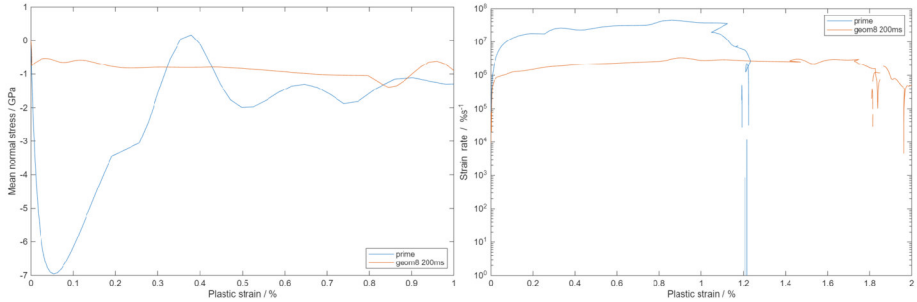

Figure 2.14: Mean normal pressure for Geometry 8 at $200\,ms^{-1}$ compared with Prime2024 experiments

outcomes confirm that controlling the mean normal stress is a viable strategy for reproducing the desired deformation regime, characterized by lower pressures and extended plastic activity.

2.5 Impact Experiments

The impact experiments were carried out using a single-stage light gas gun capable of launching a $100\,g$ projectile at a velocity of about $10^3\,\mathrm{ms}^{-1}$. The tests were performed inside a vacuum chamber, with a typical residual pressure of approximately 8 mbar, to minimize aerodynamic effects during flight. The event was recorded using a Phantom VEO 410L high-speed camera. Projectile and target velocities were monitored through an OZM PDV system, while a Siglent oscilloscope with a bandwidth of $4\,GHz$ was used for signal acquisition and synchronization (Figure 2.15).

Figure 2.16 shows the experimental setup employed for the impact tests. The configuration includes the front section of the gas gun where the jig was screwed in, the sabot with a copper flyer plate, and the complete target assembly. A thin mirror-like tape was placed in front of the target surface to reflect the laser beam for the (PDV) measurements as detailed below.

In Figure 2.17, the section of the jig assembly is reported. From left to right, the figure shows the sabot, which features two cavities designed no also to reduce its weight, but, since holes were made on the portion were the flyer was glued them allow the air to be aspirated when the vaccum pump was switched on. In this way, a secondary impact of the sabot against the flyer was avoided, as was the compression air during the collapse of the sabot itself. The flier, highlighted in red, will impact the specimen (also shown in red), which is held in place by the momentum trap (in black). The three screws located on the face of the momentum trap–specimen assembly secure the holder accommodating the PDV system (on

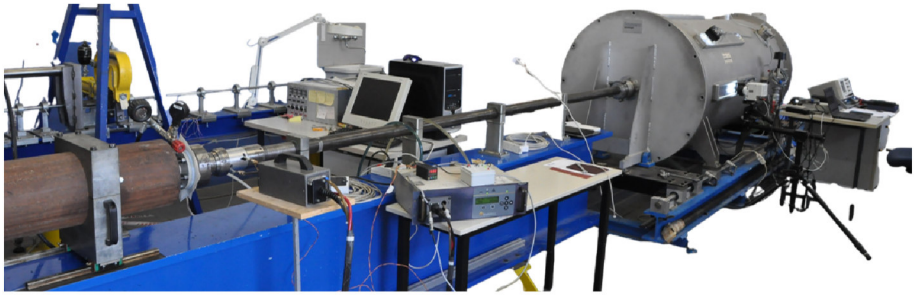

Figure 2.15: Single-stage light gas gun system.

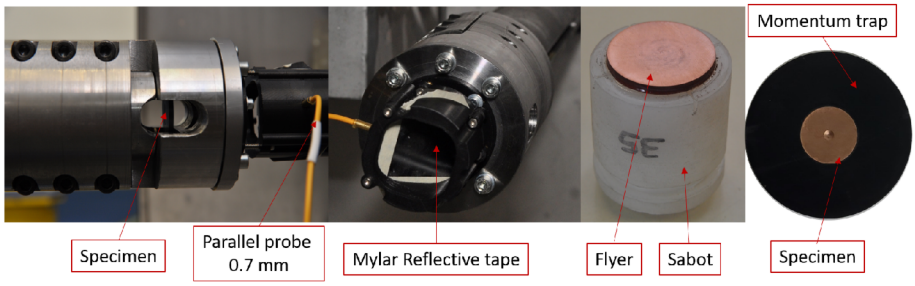

Figure 2.16: Experimental setup

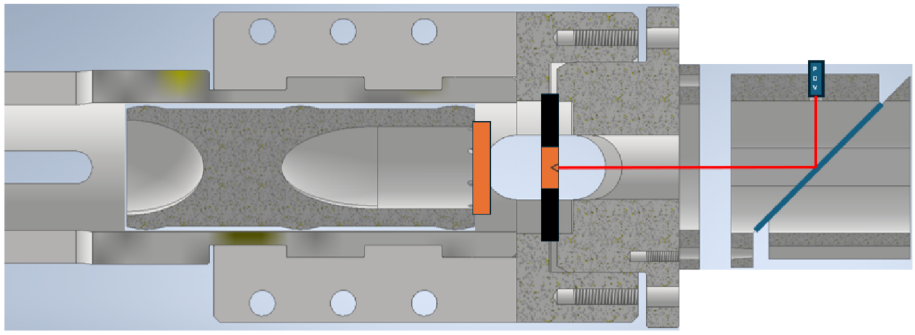

Figure 2.17: jig in section

the right). The mirror tape, shown in light blue, enables the PDV signal (indicated by the red line) to reach the specimen.

This solution allowed the velocity signal to be recorded directly from the target surface without requiring any additional reflective coating or sacrificial layer, which could otherwise be damaged or detached during the impact event. The use of this solution ensured a stable optical reflection throughout the test, maintaining signal quality while preserving the target's integrity.

Two experimental tests were conducted using geometries 5 and 8. For each geometry, two separate shots were carried out, and in all cases, the impact velocity was highly reproducible. falling within the range of 435 ± 10 m s^{-1}. Due to some alignment difficulties encountered during the setup, the velocity profile could not be successfully recorded. In particular, two main sources of misalignment were identified during the experiments and will be addressed in chapter 3:

- **Misalignment of sabot**. This is related to maintaining the proper alignment of the sabot (and consequently of the flyer attached to it) while it travels along the launch barrel.

- **Misalignment of jig**. The second issue concerns the jig, which does not efficiently dissipate the impact energy and tends to deform upon loading, thus losing the alignment of the PDV system.

Moreover, the presence of a thin oxide layer on the specimen surface caused a strong flash of light at the moment of impact, which saturated the camera sensor and prevented image acquisition from being captured. Nevertheless, post-mortem analyses have been carried out on the main fragments, the residual portion from which the spikes originated (rather than the spikes themselves, which were too small to be recovered). Optical images were acquired with a Zeiss AxioZoom optical microscope. In contrast, electron images have been acquired with a Zeiss UltraPlus Scanning Electron Microscope, equipped with an Energy Dispersive Spectroscopy (EDS) detector (Oxford X-Max) and an Electron BackScattered Diffraction detector (Oxford C-Nano).

Recovered fragments have been reported in figure 2.18, showing damage from spallation and a central pin, detached in the case of the second shot of geometry 5 (top-right in figure 2.18). As predicted by the numerical simulations, Geometry 5 did not produce any jet formation, whereas both specimens corresponding to Geometry 8 clearly exhibited jet ejection (figure 2.18). The recovered sample, shown in a 3D-reconstructed digital optical image in figure 2.19, exhibits a smooth and continuous surface morphology at the center of impact, without any sign of material ejection or localized necking that could indicate the onset of spike formation. The absence of visible protrusions or cracks confirms that the imposed conditions were below the threshold for jet initiation. The small bright area in the center of the

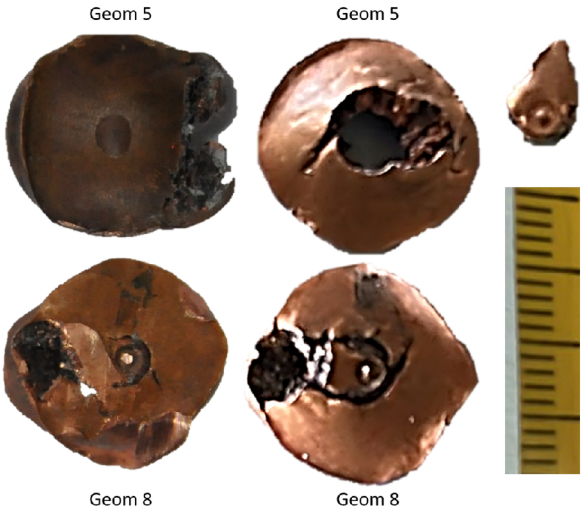

Figure 2.18: images of recovered fragments of the two geometries

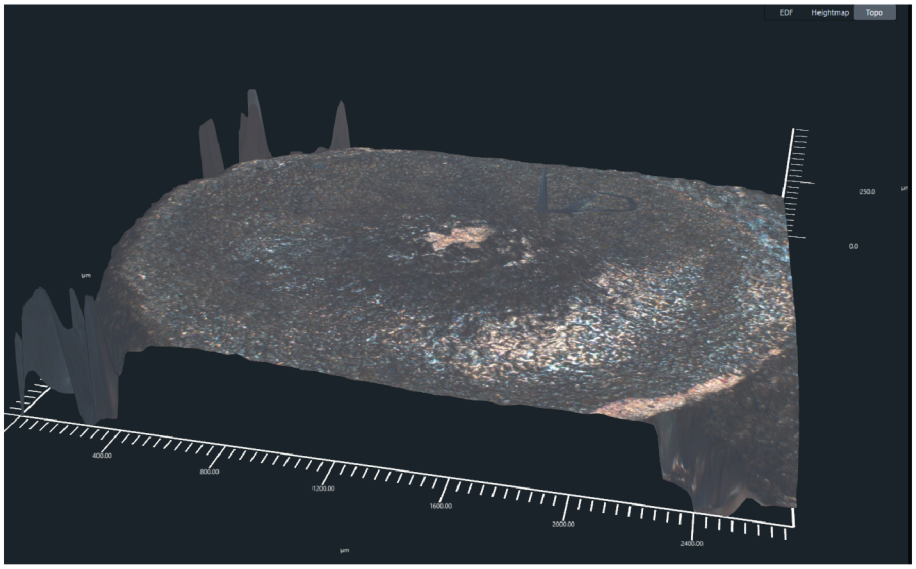

Figure 2.19: 3d reconstructed digital optical image of geometry 5, second shot, a magnification of the spike area.

spike area seems to be an area affected by mechanical interference resulting from the impact, most likely due to contact with another object before sample recovery.

Conversely, the specimen tested with Geometry 8 (Fig. 2.20) clearly shows evidence of jet formation. A distinct central protrusion is visible, approximately 0.5 millimeters in height. These morphological features are consistent with a high-strain-rate instability leading to the detachment of a narrow jet, as also predicted by the simulations. The spike and bubble area was observed in detail in electron microscopy (figure 2.21). The spike area, located at the bottom left, exhibits a different morphology compared to the bubble area. The spike area appears to show a distinct microstructure from that of the bubble region, with grains that seem to be elongated along the jet growth direction. However, based solely on SEM observations, this remains a hypothesis, as such morphology could also be confused with post-shock impact effects. A definitive confirmation will be provided in the metallographic analysis section (section 2.6). An elemental analysis was performed from spike area to bubble area and reported in figure 2.22. While counts per second (cps) of copper remain relatively constant, the oxygen content appears to increase as the transition from spike to bubble area occurs. Since the copper signal does not vary significantly, the observed rise in oxygen concentration can be attributed to an actual increase in its local content, rather than to a general enhancement of EDS counts. This interpretation is supported by the presence of oxidized dimples visible in Figure 2.23, likely formed due to the very high temperatures reached in the

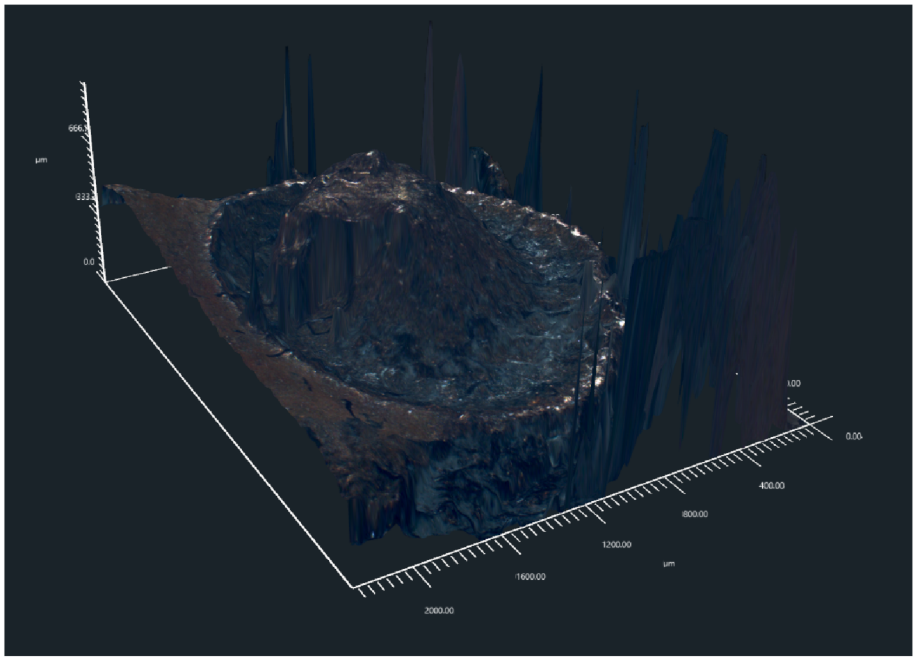

Figure 2.20: 3d reconstructed digital optical image of geometry 8, second shot, a magnification of the spike area.

sample, without any material flow replenishing the surface as occurred in the spike region.

All specimens exhibited spallation damage. While the two geometry 8 specimens appear similar, the two geometry 5 specimens show different levels and patterns of damage, which can be attributed to a slight misalignment of the samples.

This damage occurs due to the superposition of the reflection wave originating from the flyer with the tensile wave reflected at the sample surface. Because of geometric constraints and the mass of the flyer, it was not possible to shift this wave superposition within the flyer. However, this damage occurs at $t > 3$ μs, by which time the spike generation process is already underway and therefore unaffected by the spallation.

An example of this damage is highlighted in figure 2.24, where a map of stress triaxiality of geometry 8 is presented at $t = 3\mu s$ after impact. A stress triaxiality value exceeding 5 is shown, in an area of the sample compatible with spallation damage observed in 2.18. It is well known that increasing triaxiality reduces the equivalent strain required for fracture, as shown in Figure 2.25 for a stress triaxiality of 5. For annealed copper, a plastic strain of 0.1 % is enough to cause fracture. The simulation shown in Figure 2.24 indicates that plastic strain has exceeded 1 % in the spallation area.

This spallation damage has been observed using a scanning electron microscope (Figure 2.26). Both geometry 5 and geometry 8 exhibit ductile damage, originating from the nucleation, growth, and coalescence of microvoids (*dimples*). Ductile damage was observed despite the very high stress triaxiality (above 5) and the high strain rates involved in the test. This observation highlights the remarkable ductility of annealed copper, which can sustain significant plastic deformation even under severe loading conditions.

2.6 Metallographic analyses

Metallographic analyses were conducted on sectioned specimens obtained from various samples. Each specimen was mounted in epoxy resin, followed by a sequential grinding and polishing process to get a mirror-like surface. To remove as much as possible the mechanically deformed layer induced by surface preparation, the samples were chemically etched using a ferric chloride ($FeCl_3$) solution and subsequently re-polished. This additional step significantly improved the quality of the Kikuchi patterns (cf. Appendix B) obtained during the EBSD analyses.

The EBSD data will be presented in several formats to provide a comprehensive overview of the microstructural features. First, Inverse Pole Figure (IPF) maps along the y-axis will be shown. An IPF map is a representation of the crystallographic orientation of grains relative to a chosen sample direction, where each color corresponds to a specific crystal orientation. In the maps presented here, the z-direction

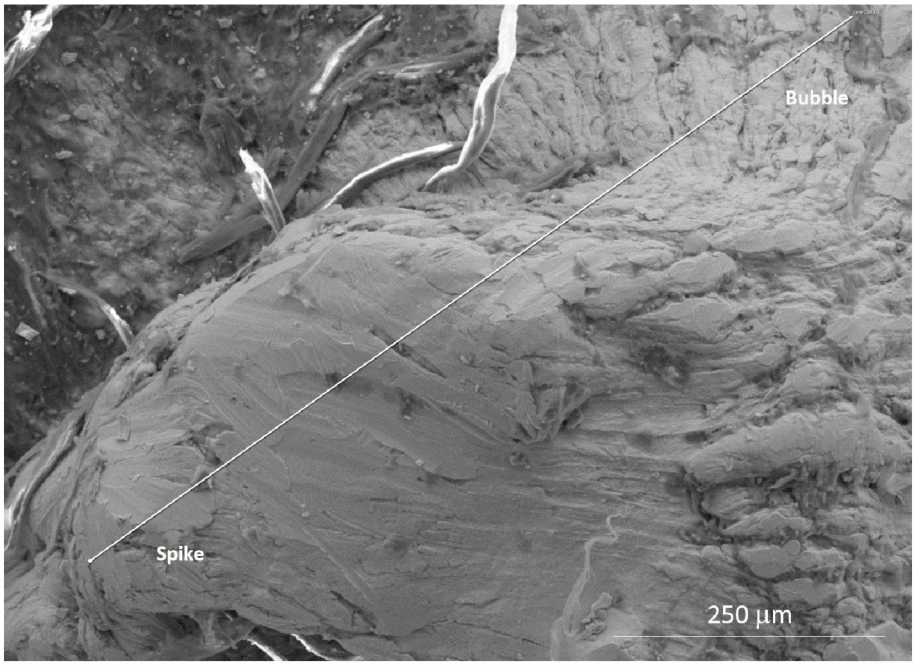

Figure 2.21: Scanning electron microscopy image of the spike and bubble region of geometry 8, second shot. The white line running from the spike to the bubble region represents the EDS line scan reported in Figure 2.22.

.

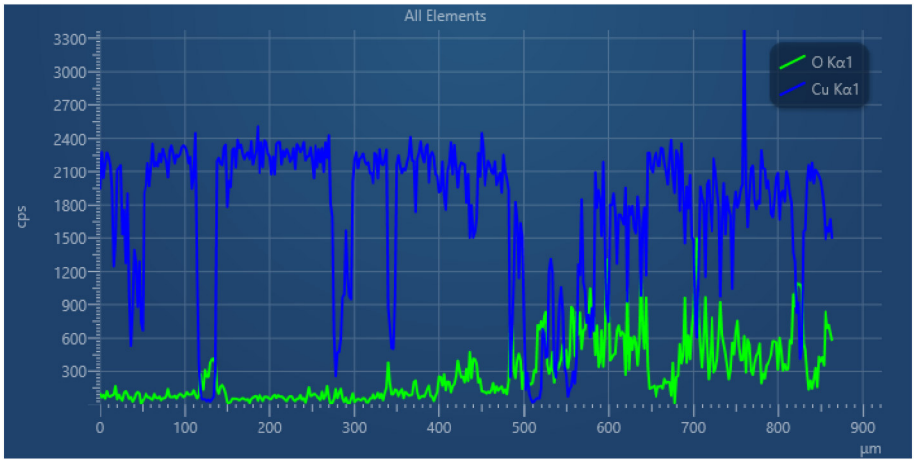

Figure 2.22: EDS line scan for copper and oxygen of spike (left) and bubble (right) area of geometry 8 sample.

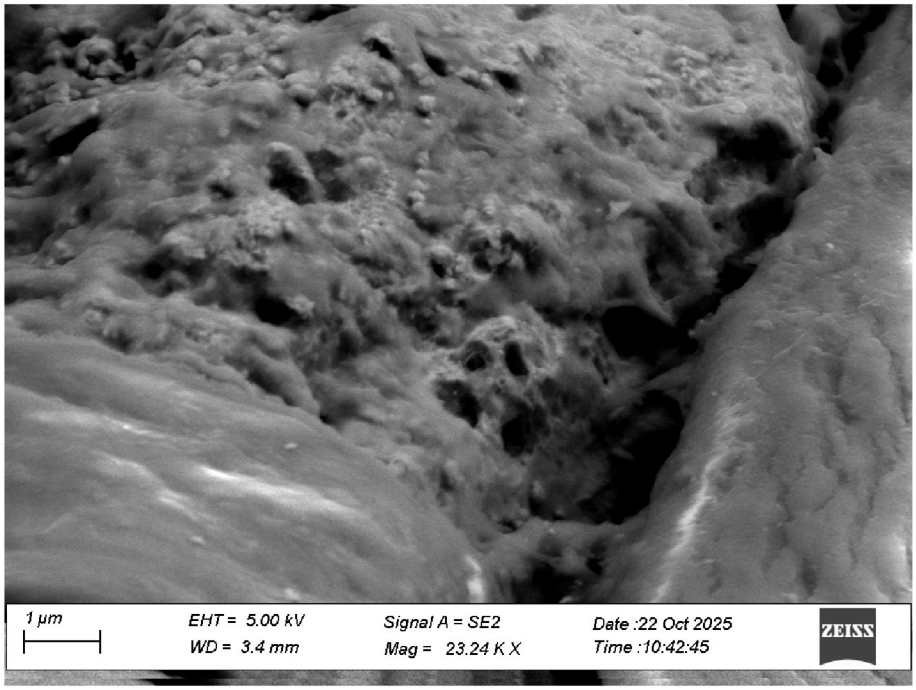

Figure 2.23: Magnification of bubble area of Geometry 8.

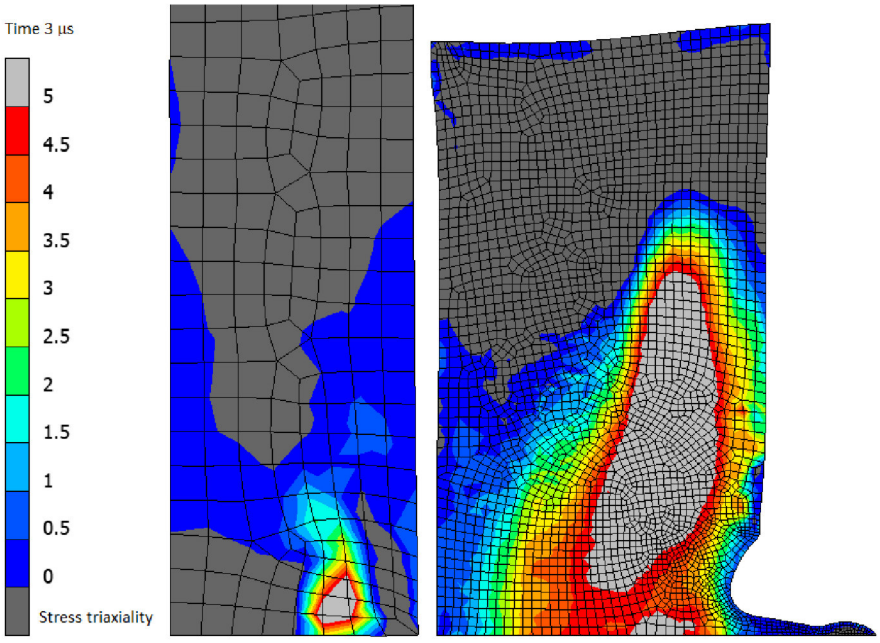

Figure 2.24: Map of stress triaxiality of geometry 8 at 3 μs after impact.

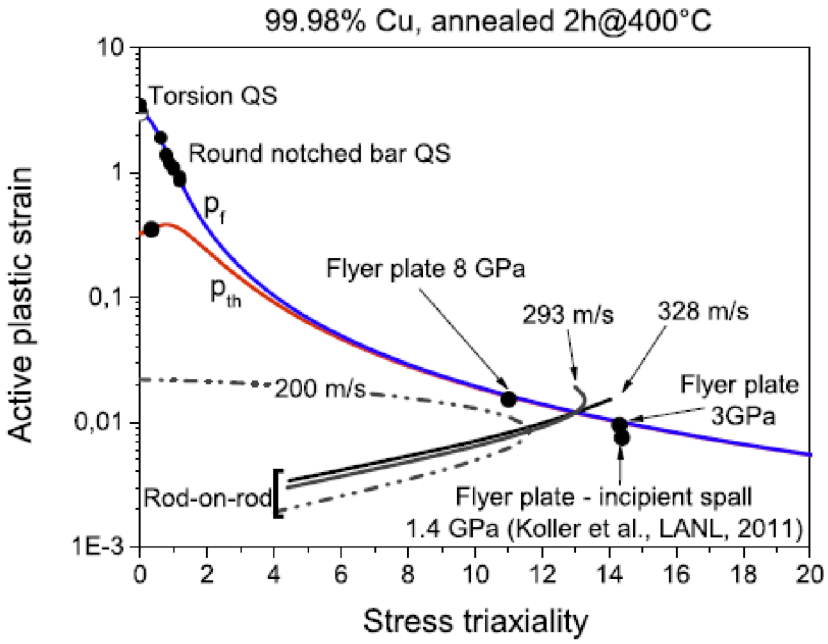

Figure 2.25: Stress triaxiality vs ductility plot [55]

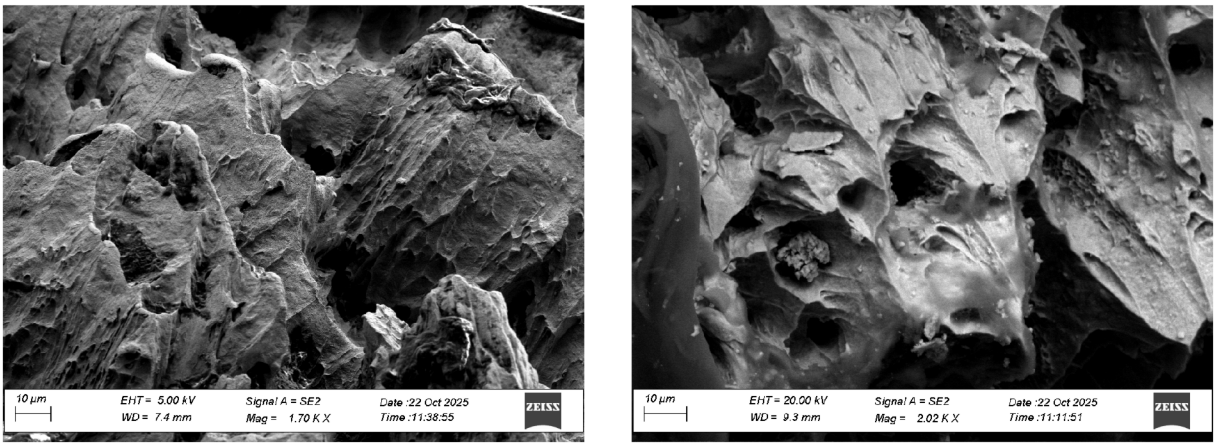

Figure 2.26: Left, damage in geometry 5 sample, right damage in geometry 8.

points out of the plane of the screen, the x-direction runs from left to right, and the y-direction runs from bottom to top. For the impact-tested samples, the extrusion direction was aligned with the y-axis for convenience during SEM positioning. The color coding of the IPF maps is shown alongside each figure. Grains with the (100) plane normal oriented along the y-axis are colored red, grains with (101) orientation are shown in green, and grains with (111) orientation are shown in blue. Orientations that lie between these principal directions are represented by intermediate colors, providing a continuous visual representation of the crystallographic orientation across the microstructure.

Since crystallographic orientations can vary along all three sample directions, IPFs are presented as heat maps along the x, y, and z axes. In each map, blue indicates that no grain exhibits that particular orientation, green represents random orientations, and red means the frequency with which a specific orientation occurs, with the exact number shown above the colour-bar legend. This visualization allows a clear assessment of the distribution of grain orientations along each principal direction.

In addition to orientation maps, the EBSD data will also be presented as Kernel Average Misorientation (KAM) maps. The KAM represents the average misorientation between a given point and its neighboring points, providing a measure of local lattice distortion and, qualitatively, the strain accumulation within the grains. For the calculation of the KAM, a cubic kernel with a size of 3×3 neighboring points was used. This kernel size allows the local misorientation to be averaged over a small neighborhood, providing a balance between sensitivity to local lattice distortions and noise reduction.

Furthermore, the microstructure will be analyzed in terms of grain boundaries. Boundaries will be

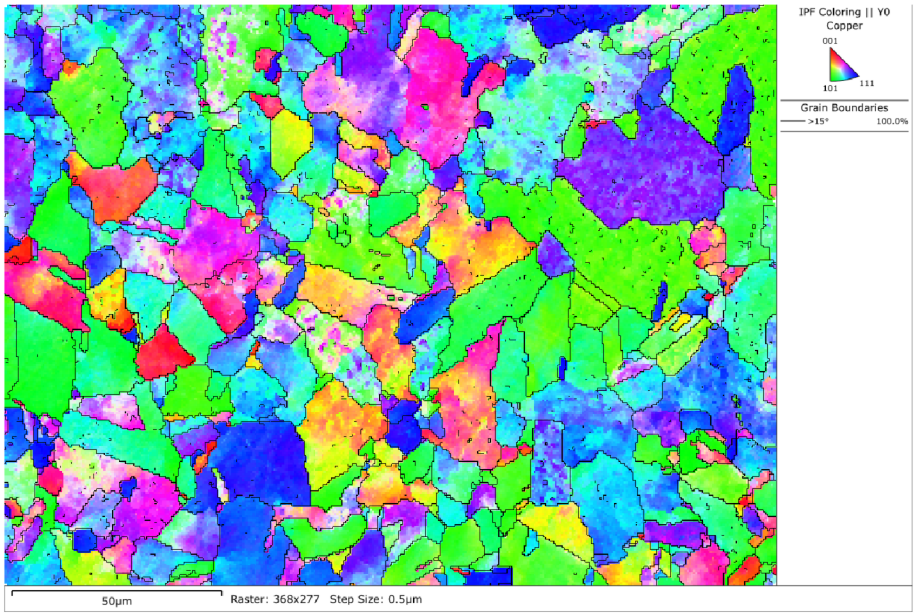

Figure 2.27: IPF map along y-axis of as-received copper

classified into low-angle boundaries (LAB), denoted by green lines, with misorientations between 2° and 10°, and high-angle boundaries (HAB), denoted by black lines, with misorientations greater than 10°. In LAB, the lattice planes of the neighboring grains are nearly aligned, and the boundary can be described as an array of dislocations that accommodate the slight misorientation. For specific combinations of misorientation axis and angle, two adjacent grains can share a certain fraction of lattice sites in identical positions. Boundaries characterized by these special orientation relationships are referred to as *coincidence boundaries*. When the fraction of coincident lattice sites is sufficiently high, such interfaces may display distinct physical behavior, for instance, an increased boundary mobility. The most fundamental example of a coincidence boundary is the twin boundary, for which the reciprocal density of coincident lattice sites, Σ, equals 3 [56]. The maximum allowable angular deviation (i.e., the tolerance angle) is calculated as:

$$\Delta\theta = \frac{15^\circ}{\Sigma}$$

where:

- $\Delta\theta$ is the tolerance angle,
- Σ is the CSL value (e.g., $\Sigma 3$, $\Sigma 9$, etc.).

Special attention will be given to $\Sigma 3$ boundaries, which will be highlighted in red in the analysis to distinguish them from random high-angle boundaries.

A sample was taken from a copper bar from which the specimens were extracted, and was labeled "as-received". In (Figure 2.27) is reported an IPF map of this sample, showing a polycrystalline microstructure with equiaxed, polygonal grains and a mild crystallographic texture. In particular, the sample showed a preferential orientation of the (111) plane in the X and Y directions (Figure 2.28, top left). This indicates that the material retains a certain degree of deformation from the bar manufacturing process.

This deformation is clearly visible in Figure 2.28, right. Most of the grain boundaries are LAB, indicating that small misorientation angles separate the majority of adjacent grains, and thus arrays of dislocations that accommodate the slight lattice misorientation between adjacent grains. The disorientation angle distribution graph, shown in Figure 2.28 (bottom left), highlights that LABs mostly separate neighboring grains (i.e., grains in contact with each other). The arithmetic mean of the grain's equivalent circle diameter (ECD) is 8.2 μm , while the peak of the count vs. ECD distribution occurs at 4.8 μm.

In Figure 2.29 is reported the IPF map of annealed copper sample. The microstructure is equiaxed, characterized by polygonal grains, with a low degree of deformation, as indicated by KAM images. The annealing process drastically reduces accumulated deformation and texture, as reported in Figure 2.30 (top left). Grain boundaries are for the majority $\Sigma 3$ boundaries, as expected after an annealing process.

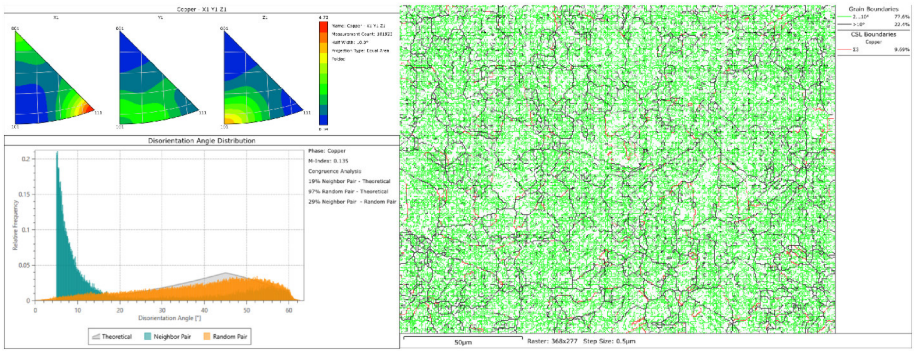

Figure 2.28: Top left, IPF over three axes, Bottom left, disorientation angle distribution, right, grain boundaries of copper as received

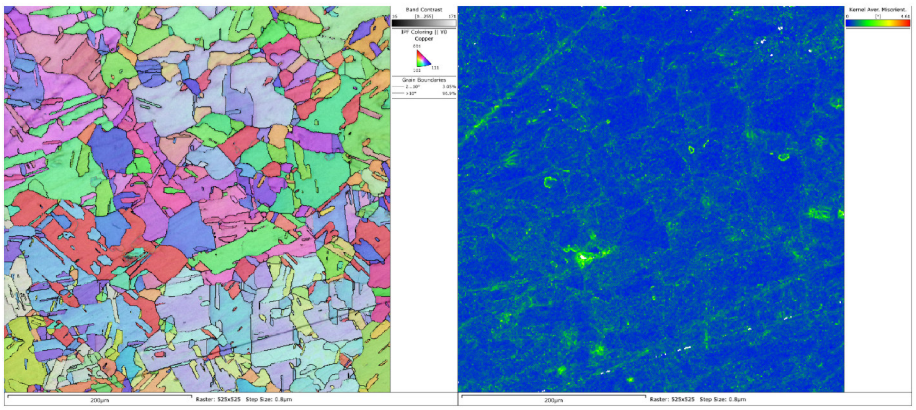

Figure 2.29: left, IPF map along y-axis sample and right KAM of annealed copper sample.

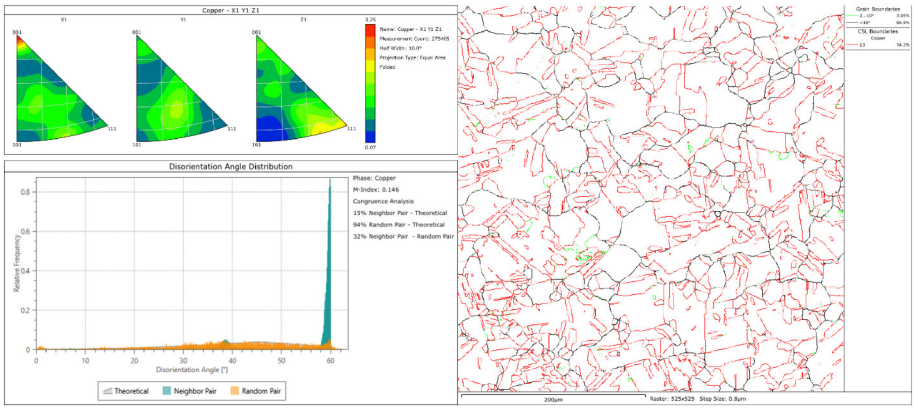

Figure 2.30: Top left, IPF over three axes, Bottom left, disorientation angle distribution, right, grain boundaries of annealed copper sample.

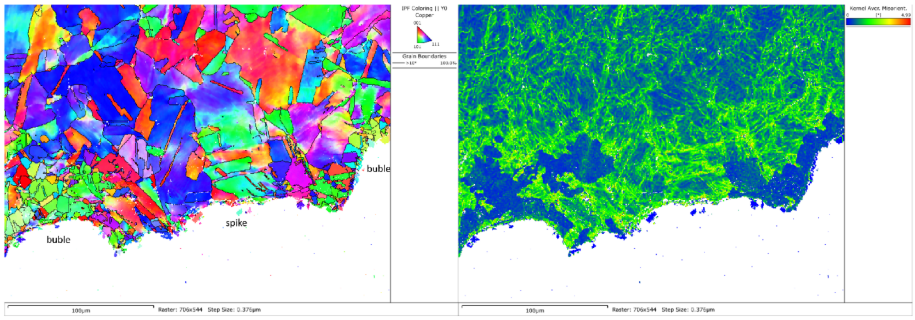

Figure 2.31: left, IPF map along y-axis sample and right KAM of geometry 5 sample.

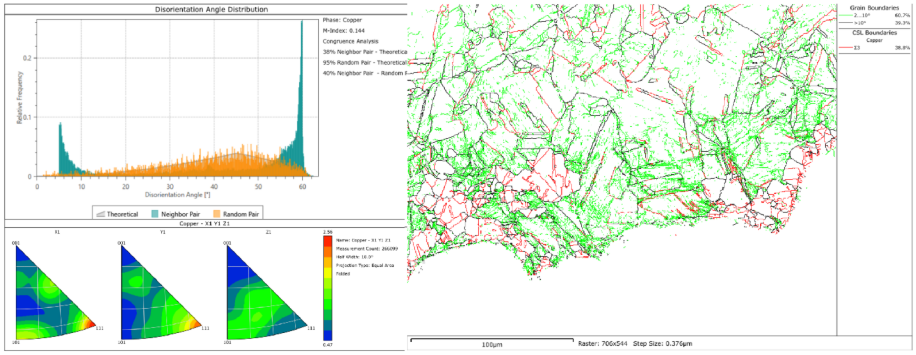

Figure 2.32: Top left, IPF over three axes, Bottom left, disorientation angle distribution, right, grain boundaries of geometry 5 sample.

Indeed, recrystallization leads to the formation of Σ3 boundaries [57]. The arithmetic mean of the grain's equivalent circle diameter (ECD) is 15.3 μm , while the peak of the count vs. ECD distribution occurs at 7.8 μm.

Geometry 5 sample IPF are reported in Figure 2.31 left. The microstructure appears equiaxed, with polygonal grains having an average equivalent circle diameter (ECD) on the order of several tens of micrometers, and the presence of twins. The microstructure far from the tip is consistent with that of annealed copper, showing a comparable grain size but a higher density of LABs, which can be attributed to the accumulation of deformation. In the two areas marked with bubbles, signs of recrystallization are evident, characterized by much smaller grains compared to annealed copper. When compared to the KAM map, shown on the right, this observation is confirmed. In the bubble-marked regions, the KAM values are close to zero (displayed in blue), indicating a low local misorientation typical of recrystallized areas. Furthermore, in the grain boundary map shown in Figure 2.32, the grain boundaries in these regions are predominantly of the Σ3 type, consistent with the expected behavior during recrystallization, without the presence of LABs in this area. LABs are still present, though less frequently than in the as-received copper, within the rest of the specimen. Additional Σ3 boundaries are also found throughout the rest of the sample, as is typical for face-centered cubic (FCC) structures, such as copper, as observed in annealed copper as well. This Σ3 peak is also visible in the misorientation angle distribution (Figure 2.32, bottom left), where a distinct peak can be observed around 60° between neighboring grains. A (111) texture is still present, although less pronounced, in the grains shown in the IPF maps along the x and y directions, as shown in Figure 2.32, bottom left.

Geometry 8 sample IPF are reported in Figure 2.33 left. The microstructure can be divided into several distinct regions. By observing the band of grains extending from the upper edge to the center of the image, one can notice that the grains appear highly elongated, with most of them exhibiting either (111) or (100) orientations. This morphology closely resembles that observed in deformed grains produced by the DTE technique [41]. In this region, the KAM map also reveals a pronounced degree of intragranular deformation. KAM images have been plotted with a maximum misorientation of 10° with respect to the other samples.

The choice of a KAM range equal to 10° for this particular region is primarily justified by the extent of the plastic deformation and the resulting high local misorientation gradients observed within the microstructure. In heavily deformed geometries, the distribution of local misorientations tends to broaden significantly due to the accumulation of geometrically necessary dislocations (GNDs) and the increased

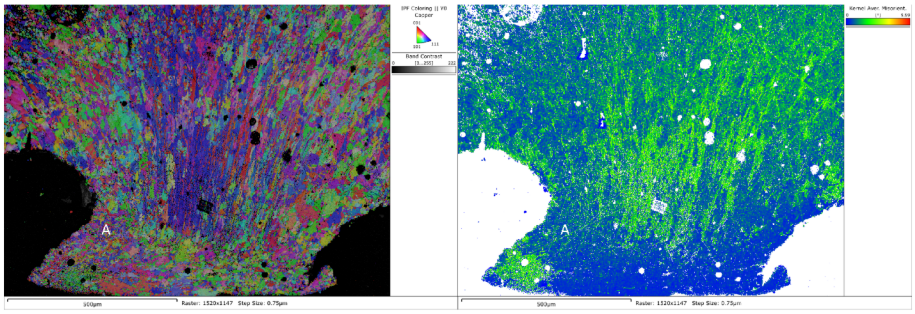

Figure 2.33: left, IPF map along y-axis sample and right KAM of geometry 8 sample.

lattice curvature associated with severe plastic strain. Using a broader KAM range (i.e., up to 10°) enables a more comprehensive and realistic representation of these local variations, thereby avoiding premature truncation of the data and ensuring that the high-misorientation tail of the distribution is adequately captured.

Conversely, in the other samples—where the deformation is less intense and the microstructure exhibits a lower degree of internal strain heterogeneity—a reduced KAM range of 5° was adopted. This narrower interval enhances sensitivity to subtle local misorientation differences that would otherwise be obscured by an unnecessarily large scale, thereby improving the contrast between regions of varying defect density.

In summary, the differentiation in KAM range between 10° and 5° reflects a deliberate adjustment to the deformation state of the samples: a broader range for highly strained geometries to capture the full extent of misorientation, and a narrower one for moderately or slightly deformed regions to emphasize fine microstructural details.

The area corresponding to the spike (Figure 2.33 exhibits features characteristic of recrystallized grains. In fact, the grains are significantly smaller than those observed in the annealed copper sample and display very low KAM values. Although it cannot be entirely excluded that grains near the tip may have experienced a secondary impact, evidence of recrystallization is also visible on the left side of the band of elongated grains, identified as region A on the map.

Moving away from the deformed area, the grain morphology gradually returns to its typical form, characteristic of the original annealed copper microstructure.

By examining the top-left panel of Figure 2.34, it is possible to observe the presence of a preferential orientation of the (111) grains along the y-axis, which corresponds to the extrusion direction of the material. This texture component is particularly pronounced in the region containing the most heavily deformed grains, which, as already discussed in previous sections, tends to develop a strong crystallographic alignment due to the high degree of plastic strain accumulated during processing. Such alignment reflects the typical deformation mechanisms active in face-centered cubic metals, where slip tends to occur preferentially along (111) planes, producing elongated grains with similar orientations. As a result, this area, characterized by a nearly single orientation, exerts a noticeable influence on the global orientation distribution of the sample. When this region is excluded from the analysis, the remaining part of the microstructure exhibits a more random texture, indicating that outside the highly deformed zone, the material retains a more equiaxed and less oriented grain structure, comparable to that of the initial annealed copper.

The plot in the bottom-left of the figure, showing the distribution of misorientation angles, further supports this interpretation. A distinct peak is visible in the region associated with low-angle boundaries (LABs) for neighboring grains, indicating a significant accumulation of geometrically necessary dislocations resulting from intense plastic deformation. In addition, a well-defined peak appears at 60°, which is typical of $\sigma 3$ grain boundaries and reveals the presence of twin-related orientations. As can be seen in the grain boundary map on the right, the recrystallized area is almost entirely populated by $\sigma 3$ boundaries, confirming that extensive twinning occurred during the recrystallization process. In contrast, the highly deformed zone is dominated by LABs, consistent with the presence of dislocation structures and subgrain boundaries formed during strain hardening. Finally, the region composed of grains that are neither strongly deformed nor recrystallized displays a balanced mixture of LABs and $\sigma 3$ boundaries, similar to what is generally observed in fully annealed copper,

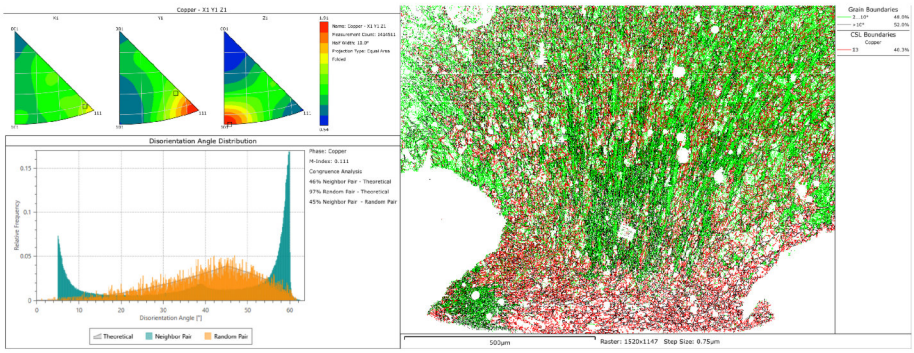

Figure 2.34: Top left, IPF over three axes, Bottom left, disorientation angle distribution, right, grain boundaries of geometry 8 sample.

Chapter 3

Discussions

The numerical and experimental investigations presented in this work were conceived to evaluate the applicability of the RMI as a diagnostic tool for assessing the mechanical response of metallic materials under high-strain-rate loading. A central aspect of this study was the systematic effort to design experimental conditions that could trigger instability while operating at significantly reduced pressure levels compared to those typically associated with conventional shock-loading techniques. This constraint was essential to allow controlled and repeatable testing while avoiding undesired hardening mechanisms related to the hydrostatic pressure, thereby isolating the contribution of the material's intrinsic mechanical behavior.

To this end, an extensive campaign of implicit finite element simulations was conducted to investigate the interplay between pressure amplitude, interface geometry, and perturbation wavelength in determining the onset and growth of the instability. The numerical results proved instrumental in defining an optimized experimental configuration, in which the shape and dimensions of the specimens were tailored to favor the development of the RMI even under moderate pressure impulses. Particular attention was devoted to identifying the minimum pressure threshold capable of inducing a measurable perturbation growth while maintaining deformation within a range compatible with the material's dynamic strength and a strain rate not lower than $10^6\,\mathrm{s}^{-1}$.

3.1 Numerical simulations

Numerical simulations played a central role in both the design and interpretation of the experimental campaign. Several different geometries were analyzed, varying their dimensionless perturbation parameter $\eta_0 k$, which governs the transition from stable deformation to jet formation. Geometries characterized by a high $\eta_0 k$ were expected to induce instability and fragmentation, whereas lower $\eta_0 k$ represented a stable configuration. With a preliminary impact velocity set to $500 ms^{-1}$, the difference between a stable and unstable configuration found was in the range $0.49 < \eta_0 k < 0.98$.

The simulations confirmed a clear inverse relationship between perturbation wavelength λ and the local strain rate $\dot{\varepsilon}$ developed during instability growth, while fragment thickness was found to scale directly with λ. These results, consistent with theoretical predictions, demonstrate that RMI can serve as a tunable platform to modulate strain rate while maintaining relatively moderate impact pressures, an essential feature for studying materials without introducing pressure-induced artifacts. Indeed, the newly proposed geometry (featuring a single large perturbation instead of multiple smaller ones) seems to achieve the goal of maintaining a sufficiently high strain rate ($> 10^6\, s^{-1}$) and large strain, while resulting in lower pressure compared to the values reported in the literature. Moreover, reducing velocity down to $200\, ms^{-1}$ with a geometry 8 sample, a $\dot{\varepsilon} > 10^6\,\mathrm{s}^{-1}$ was obtained with a $\varepsilon > 1$ and a pressure $< 1\,\mathrm{GPa}$.

3.2 Material behavior and constitutive modelling

The numerical analyses, supported by reference experimental data from Prime [47], provided significant insight into the constitutive behavior of annealed copper at strain rates approaching 10^6–$10^7\ \mathrm{s}^{-1}$. The Mechanical Threshold Stress model, calibrated on lower strain-rate data, proved capable of accurately capturing the main deformation features in this regime, confirming the robustness of physically based formulations in reproducing the interplay between strain-rate hardening and thermal softening, albeit with some limitations in simulating data beyond the strain rates for which the model was calibrated.

At high strain rates, dislocation motion becomes increasingly governed by viscous drag rather than by thermally activated processes. The MTS model correctly reproduced this transition, aligning with the theoretical formulations proposed by Follansbee [36] and Kocks [29]. Minor discrepancies were nonetheless observed in the initial growth rate of the instability, which was experimentally lower than the predicted value. This deviation is likely attributable to slight imperfections in surface flatness, boundary alignment, or local variations in the initial perturbation amplitude, factors that can substantially influence the early stages of jet development.

3.3 Experimental and numerical correlation

The experimental campaign conducted on geometries 5 and 8 provided direct validation for the numerical predictions. Despite several experimental challenges, the observed behavior qualitatively corroborated the simulations. Geometry 5 exhibited stable deformation, with no evidence of jet formation, while Geometry 8 displayed a clear onset of localized jetting and fragmentation. These findings confirm that $\eta_0 k$ effectively governs the transition between stability and instability, as theoretically anticipated.

Due to a slight misalignment between the PDV probe and the target, the velocity profiles could not be recorded. Nevertheless, post-mortem observations of the recovered specimens offered valuable qualitative confirmation of the simulated results. The geometry 5 sample retained a smooth impact surface with no visible necking or ejected material, whereas the geometry 8 fragment showed a distinct central protrusion, a typical feature of jet initiation. Such evidence demonstrates the predictive consistency of the numerical model, even in the absence of dynamic velocity measurements.

Moreover, metallurgical analysis highlights differences between these two geometries. The unstable deformation led to recrystallization, probably of a metadynamic nature, since it was not predicted by the Zener–Hollomon parameter. Conversely, the geometry 5 sample did not exhibit any recrystallization, showing a crystalline structure similar to that of the annealed material.

3.4 Experimental challenges and mitigation strategies

The experimental activity, however, also revealed several limitations that affected data acquisition and overall precision. The presence of a thin oxide film on the specimen surface generated an intense optical flash at impact, saturating the high-speed camera and preventing early-time visualization. In addition, the spike fragments produced were too small to be retrieved and analyzed, despite using perturbation wavelengths larger than those reported in the literature. Consequently, post-mortem characterization was limited to the main residual fragment, from which only qualitative evidence of jet initiation could be extracted. Finally, slight deviations in surface planarity and specimen alignment likely introduced asymmetries in the pressure field, which in turn affected the local growth of instabilities and led to differences in spallation damage among samples with the same geometry. Moreover, the sabot was probably not aligned at the time of impact with the JIG, preventing the collection of an effective PDV signal and introducing an error in the zone of the measured sample. These issues emphasize the high sensitivity of RMI tests to manufacturing accuracy, surface preparation, and diagnostic alignment. Several measures can be considered to mitigate these issues, including:

- a thorough polishing of the surfaces will be performed shortly before the experiment to address the oxide-related problems;
- a new sabot geometry can be proposed (figure 3.1, incorporating two O-rings to improve gas sealing and ensure proper alignment with the barrel;
- a completely new geometry must be reconsidered and redesigned for JIG, introducing sacrificial components that can be replaced after each shot.

The reproducibility of the experiments depends critically on interface planarity and impact alignment. Even minor angular deviations can lead to asymmetric pressure fields, modifying the local growth rate and strain distribution. Precise manufacturing and optical alignment procedures are therefore essential for reliable testing.

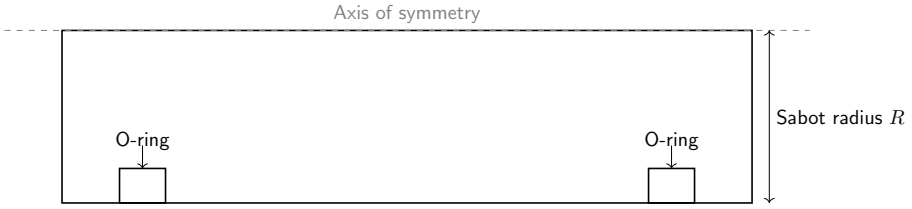

Figure 3.1: New sabot geometry proposed

3.5 Metallographic analysis

The metallographic and EBSD analyses conducted across different geometries provide a comprehensive picture of the microstructural evolution of copper subjected to varying degrees of plastic deformation and subsequent heat treatment. The comparison among the as-received material, the annealed copper, and the two impact-tested geometries (5 and 8) highlights the progressive transition from a textured and mildly deformed starting condition to a fully restored and recrystallized microstructure, and finally to a severely deformed state characterized by pronounced lattice curvature and strain localization.

The as-received copper, despite its overall polycrystalline nature, exhibits a certain degree of crystallographic texture, mainly associated with the (111) orientation. This observation suggests that residual strain and preferred orientation were retained from the initial bar manufacturing process. The predominance of low-angle boundaries (LABs) and the relative scarcity of $\sigma 3$ twin boundaries confirm that the material had not undergone a complete recrystallization and that its microstructure still reflected the presence of deformation-induced dislocation substructures.

For this reason, an additional reference specimen, here referred to as annealed copper, was prepared and analyzed. This sample was produced by subjecting copper of the same batch to a controlled annealing treatment to obtain a fully equilibrated microstructure free of the manufacturing-induced texture observed in the as-received material. The annealed copper exhibits equiaxed, polygonal grains with well-developed annealing twins and a much lower density of LABs. Its microstructural features are representative of a fully recrystallized and strain-free condition, serving as a reliable baseline for comparison. Interestingly, the morphology and boundary character distribution of this annealed copper are very similar to those observed in the non-deformed and non-recrystallized zones of geometries 5 and 8, indicating that those regions locally retained a structure akin to the annealed state, unaffected by the mechanical deformation imposed elsewhere in the sample.

The geometry 5 specimen marks the first evident deviation from this equilibrium condition. While its general grain morphology remains relatively equiaxed, specific regions display signs of local recrystallization, visible as clusters of smaller grains with near-zero KAM values. These areas correspond to strain-relieved zones formed during localized recovery and recrystallization events. The grain boundary analysis confirms the dominance of $\sigma 3$ boundaries within these regions, indicative of annealing twins typically formed during recrystallization. However, LABs persist in the rest of the sample, albeit with a lower density compared to the as-received material, similar to the annealed sample.

The geometry 8 specimen represents the most extreme microstructural state within this series. It exhibits a complex combination of deformation and recrystallization features, with a band of heavily elongated grains showing strong (111) and (100) orientations aligned with the extrusion direction. The very high local misorientation values captured in the KAM map, plotted with an extended range up to 10°, attest to the intense lattice distortion and dislocation accumulation in this region. The adoption of this broader KAM range was essential to represent the high level of local misorientation accurately and to prevent data truncation, which would otherwise obscure the most deformed features. The presence of numerous LABs in this area further supports the interpretation of a heavily strained microstructure, while the adjacent recrystallized regions, rich in $\sigma 3$ boundaries and characterized by low KAM values, confirm that local strain-induced recrystallization has occurred.

Overall, the microstructural gradient observed across the samples, from the annealed to the severely deformed condition, provides valuable insight into the interplay between deformation, recovery, and recrystallization mechanisms in copper. The annealed specimen offers an apparent structural reference, illustrating the equilibrium condition from which both deformation and recrystallization pathways diverge. The evolution from LAB-dominated to $\sigma 3$-dominated boundary networks, and the gradual textural realignment along the extrusion direction, collectively reveal the strong dependence of copper's microstructural response on strain intensity and thermal history. These findings not only clarify the

progression of microstructural changes induced by mechanical and thermal treatments but also establish a solid foundation for correlating EBSD-derived descriptors with the mechanical behavior and local strain distribution observed in subsequent analyses.

A further aspect worth considering is the apparent occurrence of metadynamic recrystallization within the most deformed regions, particularly in the geometry 8 specimen. According to the estimated values of the Zener–Hollomon parameter, the combination of strain rate and temperature experienced during the process should not have been sufficient to activate conventional static or dynamic recrystallization mechanisms. In principle, the calculated Z parameter indicated deformation conditions corresponding to a fully work-hardened state, where recovery processes would dominate over recrystallization. However, the microstructural evidence clearly suggests the presence of newly formed, strain-free grains adjacent to heavily deformed areas. This localized and incomplete grain refinement, occurring shortly after the cessation of deformation, is consistent with metadynamic recrystallization. This mechanism initiates during deformation but proceeds during the brief post-deformation stage while the material is still at an elevated temperature. The resulting microstructure, characterized by a mixed presence of elongated, deformed grains and equiaxed, recrystallized ones, provides strong indirect evidence that the residual stored energy and the transient thermal field were sufficient to trigger this process, despite predictions derived from the Zener–Hollomon analysis.

3.6 General consideration over RMI technique

The outcomes of this study confirm that RMI-based experiments can serve as a robust validation platform for constitutive models at ultra-high strain rates, bridging the gap between Split-Hopkinson bar and plate-impact techniques. By tuning the perturbation wavelength, it becomes possible to control the strain rate while maintaining moderate pressure levels, thereby isolating strain-rate effects from pressure hardening.

The satisfactory agreement between experiments and simulations validates the MTS model for describing high-rate deformation in metals. Consequently, RMI testing emerges as a promising and complementary approach for the experimental calibration and validation of physically based constitutive laws. With future improvements in diagnostic accuracy, surface preparation, and alignment control, the technique could evolve into a standard experimental framework for exploring the fundamental physics of material strength at extreme strain rates.

Summary and conclusions

This study has investigated the Richtmyer–Meshkov Instability (RMI) as a diagnostic technique for exploring the high-strain-rate response of metallic materials, combining numerical simulations with gas-gun experiments on annealed copper.

- Numerical–experimental consistency. The experiments performed on geometry 5 and geometry 8 qualitatively confirmed the simulated transition between stable and unstable configurations. Geometry 5 produced no jets, whereas geometry 8 showed clear signs of localized jetting and fragmentation, in agreement with the numerical predictions.
- Validation of the constitutive model. The MTS model, calibrated on lower-rate data, proved effective in reproducing the deformation regime observed in the experiments, demonstrating its applicability in the viscous-drag-dominated domain.
- Experimental sensitivity. The campaign revealed that even small imperfections in surface preparation and alignment can significantly affect reproducibility. Optical disturbances caused by oxide layers, along with the small fragment size, remain the main obstacles to quantitative measurements.
- RMI as a bridging technique. The present results confirm the potential of RMI-based experiments to bridge the gap between Split-Hopkinson bar and plate-impact tests, enabling strain-rate modulation at moderate pressures and providing a framework for model validation at extreme deformation rates.

Future Work

Further developments are required to enhance the experimental robustness and diagnostic precision of RMI studies:

- Surface preparation. The oxide layer should be mechanically removed immediately before testing, ensuring a clean metallic surface and minimizing optical saturation at impact.
- A new sabot geometry, incorporating O-rings for sealing and alignment, has been proposed in Chapter 3 but has to be validated experimentally. Additionally, a new JIG geometry should be developed to enhance the overall alignment further.
- Enhanced diagnostics. Future setups can employ multiple PDV channels and a fast infrared camera to track the thermal history of the sample and compare it with simulations.
- Specimen manufacturing. Tighter machining tolerances and interferometric surface inspection can be employed to minimize geometric asymmetries and enhance repeatability.
- Expanded material database. Beyond copper, future work will extend to alloys and anisotropic materials to evaluate how microstructural features influence the growth of instability under comparable impact conditions.

By addressing these limitations, future RMI experiments will enable quantitative validation of constitutive laws at high strain rates, consolidating this methodology as a powerful tool in the study of dynamic material behavior.

Bibliography

[1] Linan Su and Hamid Roshan. "Mechanisms of strain rate-dependent response of naturally fractured coal". In: *International Journal of Coal Geology* 300 (2025), p. 104711. DOI: 10.1016/j.coal.2025.104711.

[2] Guolin Ren, Honglu Fei, and Kun Chen. "Determination and Verification of HJC Model Parameters for Lead Zinc Ore Surrounding Rock". In: *Proceedings of the 10th International Conference on Architectural, Civil and Hydraulic Engineering (ICACHE 2024)*. 2024. DOI: 10.2991/978-94-6463-658-1_80.

[3] Batuhan Alicioglu, Ugur Can, and Ibrahim Guven. "High Performance Materials for Extreme Environments". In: *AIAA Scitech Forum*. 2025. DOI: 10.2514/6.2025-0134.

[4] Xinjun Wang et al. "Dynamic Response Analysis of Bird Strike on Aircraft Windshield Based on Damage-modified Nonlinear Viscoelastic Constitutive Relation". In: *Chinese Journal of Aeronautics* 20 (2007), pp. 511–517.

[5] G.S. Langdon and W.J. Cantwell. "Impact and Blast Loading of Composites". In: *Woodhead Publishing Series in Composites Science and Engineering*. Woodhead Publishing, 2020, pp. 415–439. DOI: 10.1016/B978-0-08-102679-3.00014-9.

[6] Lee S. Magness Jr. "High strain rate deformation behaviors of kinetic energy penetrator materials during ballistic impact". In: *Mechanics of Materials* 17.2-3 (1994), pp. 147–154. DOI: 10.1016/0167-6636(94)90055-8.

[7] R. Betti et al. "Shock Ignition of Thermonuclear Fuel with High Areal Density". In: *Physical Review Letters* 98 (2007), p. 155001. DOI: 10.1103/PhysRevLett.98.155001.

[8] J.C. Raymond. "Shock Waves in Supernova Ejecta". In: *Space Science Reviews* 214.28 (2018). DOI: 10.1007/s11214-017-0453-6.

[9] E. Zullo et al. "Groundwater flow numerical analysis of the Sibillini Hydrostructure (Central Italy): system characterization and evaluation of hydrogeological changes after the Mw 6.5 Norcia earthquake". In: *Italian Journal of Engineering Geology and Environment* (2024), pp. 295–304. DOI: 10.4408/IJEGE.2024-01.S-32.

[10] H. Kolsky. "An Investigation of the Mechanical Properties of Materials at Very High Rates of Loading". In: *Proceedings of the Physical Society. Section B* 62.11 (1949), p. 676. DOI: 10.1088/0370-1301/62/11/302.

[11] Daniel Casem. "Dynamic Material Testing: Split Hopkinson Bar Techniques". In: *Advances in Experimental Impact Mechanics*. 2022, pp. 149–189.

[12] Marc A. Meyers. *Dynamic Behavior of Materials*. Wiley-Interscience, 1994.

[13] G.T. Gray et al. "Shock Compression of Condensed Matter". In: *Proceedings of the Conference of the American Physical Society Topical Group on Shock Compression of Condensed Matter*. 2006, pp. 725–728.

[14] E. Orowan. "Zur Kristallplastizität. III". In: *Zeitschrift für Physik* 89 (1934), pp. 634–659.

[15] M. Polanyi. "Über eine Art Gitterstörung, die einen Kristall plastisch machen könnte". In: *Zeitschrift für Physik* 89 (1934), pp. 660–664.

[16] G.I. Taylor. "Mechanism of Plastic Deformation in Crystals". In: *Proceedings of the Royal Society of London. Series A* 145 (1934), pp. 362–387.

[17] P. Ludwik. *Element der Technologischen Mechanik*. Springer, 1909.

[18] R. Peierls. "The Size of a Dislocation". In: *Proceedings of the Physical Society* 52 (1940), pp. 34–37.

[19] E.O. Hall. "The Deformation and Ageing of Mild Steel: III Discussion of Results". In: *Proceedings of the Physical Society. Section B* 64 (1951), pp. 747–753.

[20] N.J. Petch. "The Cleavage Strength of Polycrystals". In: *Journal of the Iron and Steel Institute* 173 (1953), pp. 25–28.

[21] R.L. Fleischer. "Substitutional Solution Hardening". In: *Acta Metallurgica* 11 (1963), pp. 203–209.

[22] Peter F. Follansbee and G.T. Gray. *Fundamentals of Strength*. Wiley, 2014.

[23] H. Widersich. "Hardening mechanisms and the theory of deformation". In: *J. Metals* 16 (1963), pp. 423–428.

[24] R. W. K. Honeycombe. *The Plastic Deformation of Metals*. Edward Arnold, 1968.

[25] R. L. Fleischer. "Solid solution hardening". In: *Acta Metallurgica* 11 (1963), pp. 203–209. DOI: 10.1016/0001-6160(63)90213-X.

[26] E. Voce. "The Relationship between Stress and Strain for Homogeneous Deformation". In: *Journal of the Institute of Metals* 74 (1948), pp. 537–562.

[27] Y. V.R.K. Prasad and K.P. Rao. "Kinetics and dynamics of hot deformation of OFHC copper in extended temperature and strain rate ranges". In: *International Journal of Materials Research* 96.1 (2005), pp. 71–77. DOI: 10.3139/ijmr-2005-0010.

[28] M.O. Peach and J.S. Koehler. "The Forces Exerted on Dislocations and the Stress Fields Produced by Them". In: *Physical Review* 80 (1950), pp. 436–439. DOI: 10.1103/PhysRev.80.436.

[29] U. F. Kocks. "Laws for Work-Hardening and Low-Temperature Creep". In: *Journal of Engineering Materials and Technology* 77 (1976).

[30] G.R. Johnson and W.H. Cook. "A Constitutive Model and Data for Metals Subjected to Large Strains, High Strain Rates, and High Temperatures". In: *Proceedings of the 7th International Symposium on Ballistics*. The Hague, 1983, pp. 541–547.

[31] O.A. Bauchau and J.I. Craig. "Constitutive Behavior of Materials". In: *Structural Analysis. Solid Mechanics and Its Applications*. Vol. 163. Springer, 2009, pp. 155–186. DOI: 10.1007/978-90-481-2516-6_2.

[32] F.J. Zerilli and R.W. Armstrong. "Dislocation-mechanics-based Constitutive Relations for Material Dynamics Calculations". In: *Journal of Applied Physics* 61 (1987), pp. 1816–1825.

[33] P.S. Follansbee and U.F. Kocks. "A constitutive description of the deformation of copper based on the use of the mechanical threshold stress as an internal state variable". In: *Acta Metallurgica* 36.1 (1988), pp. 81–93. ISSN: 0001-6160. DOI: https://doi.org/10.1016/0001-6160(88)90030-2. URL: https://www.sciencedirect.com/science/article/pii/0001616088900302.

[34] D.L. Preston, D.L. Tonks, and D.C. Wallace. "Model of Plastic Deformation for Extreme Loading Conditions". In: *Journal of Applied Physics* 93.4 (2003), pp. 2118–2131.

[35] A. Molinari and G. Ravichandran. "A Phenomenological Constitutive Model for High Strain-rate Deformation in Metals Based on the Evolution of an Effective Microstructural Length". In: *Mechanics of Materials* 37.7 (2005), pp. 737–752.

[36] P.S. Follansbee. "The Rate Dependence of Structure Evolution in Copper and Its Influence on the Stress-Strain Behavior at Very High Strain Rates". In: *Impact Loading and Dynamic Behaviour of Materials*. Ed. by C.Y. Chiem, H.-D. Kunze, and L.W. Meyer. Informationsgesellschaft Verlag, Oberursel, 1988, pp. 315–322.

[37] J. R. Lund and J. P. Byrne. "Leonardo Da Vinci's tensile strength tests: implications for the discovery of engineering mechanics". In: *Civil Engineering and Environmental Systems* 00 (2000), pp. 1–8.

[38] John Hopkinson. "Further experiments on the rupture of iron wire". In: *Proceedings of the Manchester Literary and Philosophical Society* 11 (1872), pp. 119–121.

[39] Bertram Hopkinson. "A Method of Measuring the Pressure Produced in the Detonation of High Explosives or by the Impact of Bullets". In: *Philosophical Transactions of the Royal Society of London. Series A, Containing Papers of a Mathematical and Physical Character* 213 (1914), pp. 437–456. DOI: 10.1098/rsta.1914.0010.

[40] Richard M. Davies. "A critical study of the Hopkinson pressure bar". In: *Philosophical Transactions of the Royal Society of London. Series A, Mathematical and Physical Sciences* 240 (1948), pp. 375–457. DOI: 10.1098/rsta.1948.0001.

[41] N. Bonora, G. Testa, A. Ruggiero, et al. "Numerical Simulation of Dynamic Tensile Extrusion Test of OFHC Copper". In: *Journal of Dynamic Behavior of Materials* 1 (2015), pp. 136–152. DOI: 10.1007/s40870-015-0013-7.

[42] Xu Guo et al. "Shock-tube studies of single- and quasi-single-mode perturbation growth in Richtmyer–Meshkov flows with reshock". In: *Journal of Fluid Mechanics* 941 (2022), A65. DOI: 10.1017/jfm.2022.357. eprint: https://www.cambridge.org/core/journals/journal-of-fluid-mechanics/article/shocktube-studies-of-single-and-quasisinglemode-perturbation-growth-in-richtmyermeshkov-flows-with-reshock/9BCDC7F6C16E92ABF19EAA7120B159B0.

[43] R. D. Richtmyer. "Taylor instability in finite amplitude". In: *Los Alamos Scientific Laboratory Report LA-2432* (1960).

[44] E. E. Meshkov. "Instability of the interface of two gases accelerated by a shock wave". In: *Fluid Dynamics* 4.5 (1969), pp. 101–103.

[45] A. R. Piriz, J. J. López Cela, and N. A. Tahir. "Richtmyer–Meshkov instability as a tool for evaluating material strength under extreme conditions". In: *Nuclear Instruments and Methods in Physics Research Section A: Accelerators, Spectrometers, Detectors and Associated Equipment* 606.1–2 (2009), pp. 139–141. DOI: 10.1016/j.nima.2009.03.027.

[46] G. Dimonte et al. "Use of the Richtmyer-Meshkov instability to infer yield stress at high-energy densities". In: *Physical Review Letters* 107.26 (2011), p. 264502. DOI: 10.1103/PhysRevLett.107.264502.

[47] M.B. Prime et al. "Article title not provided". In: *Physical Review E* 109 (2024), p. 015002.

[48] Z. Rosenberg et al. "On the upturn phenomenon in the strength vs. strain-rate relations of metals". In: *International Journal of Solids and Structures* 176–177 (2019), pp. 185–190. DOI: 10.1016/j.ijsolstr.2019.04.003. URL: https://doi.org/10.1016/j.ijsolstr.2019.04.003.

[49] M.B. Prime et al. "Acta Materialia". In: *Acta Materialia* 231 (2022), p. 117875. DOI: 10.1016/j.actamat.2022.117875.

[50] B.J. Lee et al. "Constitutive Modeling of Materials under High Strain-rate Deformation". In: *Metallurgical and Materials Transactions A* 28 (1997), pp. 113–123.

[51] S. Ricci et al. "On The Role of Constitutive Modeling and Computational Parameters in the Numerical Simulation of Dynamic Tensile Extrusion Test". In: *Journal of Dynamic Behavior of Materials* 8 (2022), pp. 453–472. DOI: 10.1007/s40870-022-00352-9.

[52] John H. Carpenter. *A New Equation of State for Copper*. Tech. rep. SAND2021-11440. Computational Multiscale (01444), jhcarpe@sandia.gov. Albuquerque, NM 87185-1323: Sandia National Laboratories, 2021.

[53] M. Hörnqvist et al. "Deformation and texture evolution of OFHC copper during dynamic tensile extrusion". In: *Acta Materialia* 89 (2015), pp. 163–180. DOI: 10.1016/j.actamat.2015.02.010. URL: https://doi.org/10.1016/j.actamat.2015.02.010.

[54] Norio Furushiro, Yōzō Okada, and Shigetoku Hori. "Dynamic recrystallization during tensile deformation of copper". In: *Journal of the Society of Materials Science, Japan* 29.323 (1980), pp. 776–781. DOI: 10.2472/jsms.29.776. URL: https://www.jstage.jst.go.jp/article/jsms1963/29/323/29_323_776/_article.

[55] Gianluca Iannitti et al. "Ductile damage in Taylor-anvil and rod-on-rod impact experiment". In: *AIP Conference Proceedings* 1793 (2017), p. 100017. DOI: 10.1063/1.4971642. URL: https://doi.org/10.1063/1.4971642.

[56] D. G. Brandon. "The Structure of High-Angle Grain Boundaries". In: *Acta Metallurgica* 14.11 (1966), pp. 1479–1484. DOI: 10.1016/0001-6160(66)90168-4. URL: https://doi.org/10.1016/0001-6160(66)90168-4.

[57] Valerie Randle, Mark Caul, and Jörn Fiedler. "Twinning and Interfacial Planes in Copper". In: *Microscopy and Microanalysis* 3.3 (May 1997), pp. 224–233. DOI: 10.1017/S1431927697970173. URL: https://doi.org/10.1017/S1431927697970173.

Appendices

Appendix A

Miller Indices

A.1 Introduction

Miller indices are a notation system used in crystallography to describe the orientation of crystallographic planes and directions within a crystal lattice, providing a standardized way to identify and compare atomic arrangements, slip systems, and texture components observed through experimental or numerical analyses.

Understanding Miller indices is particularly relevant when interpreting the microstructure of a metal after deformation, recrystallization, or annealing, since many mechanical and physical properties of metals are crystallographically dependent.

A.2 The Reciprocal Lattice

To fully understand the meaning of Miller indices and their geometrical interpretation, it is essential to introduce the concept of the *reciprocal lattice*. The reciprocal lattice is a mathematical construct that represents the periodicity of a crystal in reciprocal (Fourier) space. It emerges from the Fourier transform of the lattice associated with the arrangement of the atoms. The reciprocal lattice represents the set of all wavevectors that produce plane waves maintaining the same phase across all lattice points in real space. It is not a physical lattice of atoms, but a lattice in which each point corresponds to a set of crystal planes in real space.

A.3 Definition of Miller Indices

Miller indices are represented by a triplet of integers (hkl) that define the orientation of a crystallographic plane in the reciprocal lattice. They are determined by taking the reciprocals of the intercepts that a given plane makes with the crystallographic axes and then reducing them to the smallest set of integers.

In a cubic system such as that of copper, the steps for determining Miller indices are as follows:

1. Identify where the chosen plane intercepts the crystal axes, at points named $x = a$, $y = b$, and $z = c$.
2. Take the reciprocals of the intercepts: $\left(\frac{1}{a}, \frac{1}{b}, \frac{1}{c}\right)$.
3. Multiply each term by the least common multiple to obtain integers.
4. Enclose the integers in parentheses: (hkl).

For example, a plane intercepting the axes at a, $b/2$, and $c/3$ will have reciprocals $(1, 2, 3)$, giving the Miller index (123). If a plane does not intercept an axis, for example, a plane parallel to y and z, the intercepts will be $b = c = \infty$ and the reciprocal will be 0, giving the plane (100) in case of $a = 1$. A negative index is indicated by placing a bar above the corresponding number. For example:

$$(\bar{1}00), \quad [\bar{1}10], \quad (\bar{1}\,\bar{1}1)$$

Different types of brackets (as reported above) are adopted to clearly distinguish between single planes, directions, and families of equivalent planes or directions. Table A.1 summarizes the standard conventions.

Table A.1: Notation of planes, directions, and families of planes using Miller indices.

Type	Meaning	Example	Description
(hkl)	Single plane	(111)	Refers to one specific crystallographic plane.
$[uvw]$	Single direction	[111]	A vector pointing along a specific direction.
$\{hkl\}$	Family of equivalent planes	$\{111\}$	All planes symmetrically equivalent to (111).
$\langle uvw \rangle$	Family of equivalent directions	$\langle 111 \rangle$	All directions equivalent to [111].

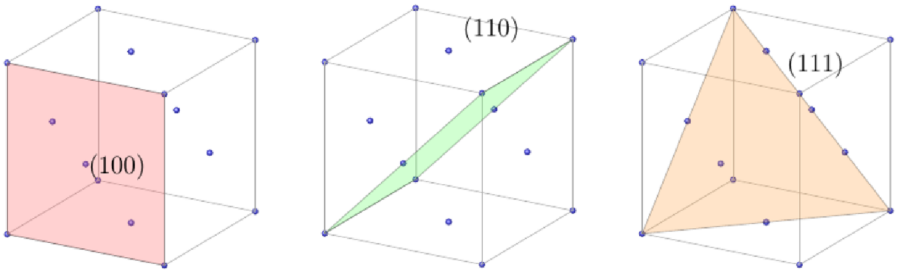

Figure A.1: (100) (110) and (111) planes for a FCC lattice.

Examples in FCC Copper

Copper has a face-centered cubic (FCC) structure, for which the following examples apply (figure A.1):

- **Plane** (111)**:** The densest atomic plane in FCC copper, often observed in electron diffraction patterns.
- **Direction** [110]**:** Lies in the (111) plane and corresponds to one of the primary slip directions during plastic deformation.
- **Family** $\{111\}$**:** Includes the four equivalent planes (111), $(\bar{1}11)$, $(1\bar{1}1)$, and $(11\bar{1})$.
- **Family** $\langle 110 \rangle$**:** Includes all equivalent directions such as [110], $[\bar{1}10]$, [101], and $[10\bar{1}]$.

These slip systems are crucial for understanding the mechanical response of copper and other FCC metals under deformation.

Relation Between Planes and Directions

In cubic crystals (such as copper), the plane (hkl) is always **perpendicular** to the direction $[hkl]$. This correspondence simplifies the interpretation of crystallographic orientations. However, in non-cubic systems, this relation does not necessarily hold.

Appendix B

Kikuchi Lines

B.1 Introduction

Kikuchi lines are characteristic diffraction features observed in electron diffraction patterns, particularly in *electron backscatter diffraction* (EBSD) or *transmission electron microscopy* (TEM). They appear as pairs of bright and dark bands, forming a complex network of intersecting lines that correspond to the crystallographic planes of the sample.

In copper and other face-centered cubic (FCC) materials, Kikuchi patterns provide direct and precise information about the crystal orientation and lattice symmetry. They represent a powerful tool to correlate real-space microstructural observations with reciprocal-space crystallography.

B.2 Formation Mechanism

Kikuchi lines originate from the *diffuse scattering* of high-energy electrons interacting with a crystalline material. The process occurs in two main steps:

1. **Inelastic scattering:** Incident electrons undergo multiple inelastic interactions with the crystal lattice, losing part of their energy and being randomly diffused inside the crystal. This generates a nearly isotropic source of scattered electrons within the material (background).

2. **Elastic diffraction:** Some of these diffusely scattered electrons are then elastically diffracted by lattice planes according to Bragg's law:

$$2d_{hkl} \sin\theta = n\lambda. \tag{B.1}$$

   where d_{hkl} is the interplane distance of that particular family of planes, θ is the incident angle, n is an integer, and λ is the wavelength of the incident electrons. Constructive interference occurs when the diffracted wave satisfies the Laue condition:

$$\mathbf{k}' - \mathbf{k} = \mathbf{G}_{hkl}, \tag{B.2}$$

   where $\mathbf{G}_{hkl}$ is a reciprocal lattice vector corresponding to the family of planes (hkl), and k and k' are respectively incident and diffracted wave vectors.

The superposition of all diffracted wavefronts from different orientations of $\mathbf{G}_{hkl}$ gives rise to two cones of enhanced and reduced intensity. When these cones intersect the detector (e.g., the phosphor screen or EBSD camera), they appear as paired bright and dark lines — the Kikuchi lines.

B.3 Geometrical Interpretation

Each Kikuchi line corresponds to the trace of a diffracting plane (hkl) on the detector. The angular separation between two lines in a pair is twice the Bragg angle $2\theta_{hkl}$, which depends on the interplanar spacing d_{hkl}:

$$2\theta_{hkl} = 2\arcsin\left(\frac{\lambda}{2d_{hkl}}\right). \tag{B.3}$$

The intersection of two Kikuchi bands corresponds to the zone axis of the crystal, which is the direction common to both planes. In terms of Miller indices, if two bands correspond to planes $(h_1k_1l_1)$ and $(h_2k_2l_2)$, their intersection represents the crystallographic direction:

$$[uvw] = (h_1k_1l_1) \times (h_2k_2l_2). \tag{B.4}$$

For instance, in FCC copper:

- The intersection of {111} and {200} Kikuchi bands defines the ⟨110⟩ zone axis.
- The {220} lines intersecting with {111} also define the same ⟨110⟩ direction, depending on the orientation of the crystal.

B.4 Relationship with the Reciprocal Lattice

The Kikuchi pattern can be directly interpreted as a projection of the reciprocal lattice onto a two-dimensional plane (the detector surface). Each Kikuchi line corresponds to the locus of reciprocal lattice points that satisfy the diffraction condition for a given (hkl) plane.

In this sense:

- The *position* of Kikuchi bands depends on the geometry of the reciprocal lattice of copper.
- The *spacing* between bands reflects the interplanar distances d_{hkl}.
- The *intersection points* correspond to zone axes — directions in the reciprocal lattice that pass through multiple lattice points.

Therefore, the Kikuchi pattern provides a real experimental image of the reciprocal lattice geometry. It can be seen as a *projection of reciprocal-space vectors* $\mathbf{G}_{hkl}$, allowing the direct determination of crystal orientation in EBSD.

B.5 Kikuchi Patterns in FCC Copper

In copper, which crystallizes in the face-centered cubic structure, the Kikuchi pattern displays high symmetry and well-defined families of bands corresponding to the major planes:

- {111} planes: the most intense bands, corresponding to the densest atomic planes.
- {200} planes: less intense but easily recognizable and perpendicular to the cube axes.
- {220} planes: often appear as narrower lines, intersecting at 60° with {111}.

A typical Kikuchi pattern from copper includes several intersections forming the ⟨110⟩ and ⟨111⟩ zone axes, as shown schematically in Figure B.1.

B.6 Experimental Observation

In an EBSD experiment, Kikuchi lines arise when an electron beam impinges on a polished copper surface tilted at approximately 70° relative to the incident beam. The backscattered electrons form a diffraction pattern on the phosphor screen behind the sample, containing numerous Kikuchi bands.

Each Kikuchi band corresponds to a specific family of planes (hkl), and by indexing these bands using the known reciprocal lattice geometry, the crystallographic orientation of each scanned point can be determined. This forms the basis of orientation mapping in EBSD.

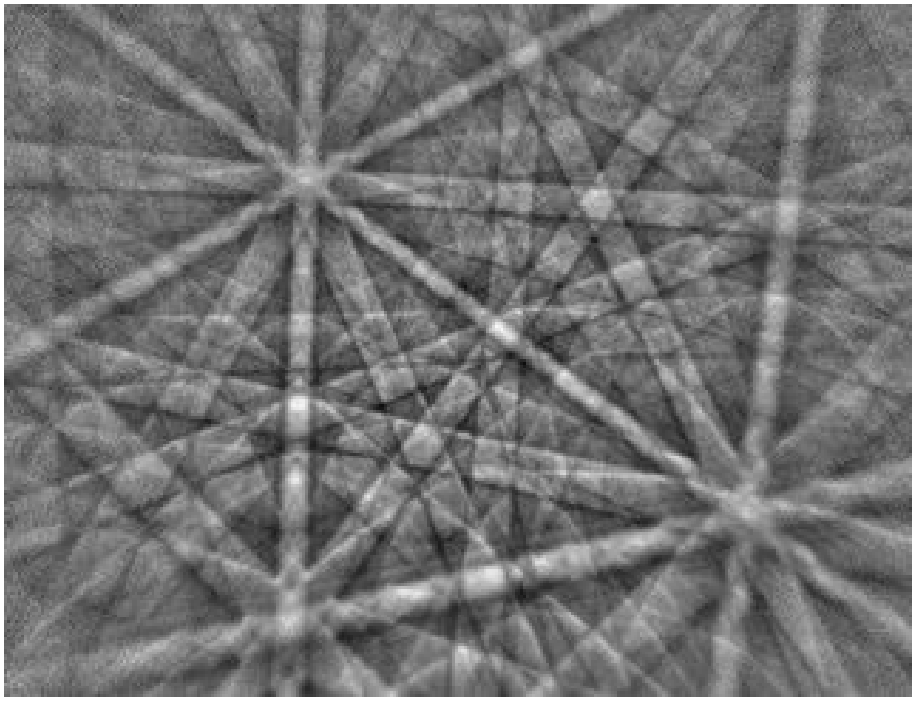

Figure B.1: Example of a Kikuchi pattern in FCC copper, showing the {111}, {200}, and {220} bands and their intersections corresponding to ⟨110⟩ and ⟨111⟩ zone axes.